Politecnico di Torino

Master’s Degree in Mechanical Engineering
A.a. 2024/2025
October 2025

Metal Matrix Composites for Aerospace Produced by Additive Manufacturing

Supervisors:
Prof. Alberta AVERSA
Prof. Federica BONDIOLI
Prof. Elisa PADOVANO

Candidate:
Esra AKILLI

Abstract

This study explores the characterization of (A2618+Ti+B) multimaterial systems created by Directed Energy Deposition (DED). Test samples that were printed using different sets of machine process parameters (scanning speed, hatching distance, and layer thickness). Key techniques for porosity investigation using optical microscopy with ImageJ software and examining the microstructure using a scanning electron microscope.

In general, while higher power levels generally increased the total pore area, scanning speed, and LED were found to strongly affect pore density, indicating the importance of evaluating both metrics to accurately describe defect evolution. SEM and EDS analyses identified the presence of TiB_2 particles and Al-based intermetallic compounds (Al-Cu, Al-Ni, Al-Fe), which played a critical role in microstructural development. TiB_2 particles contributed to grain refinement but also promoted localized pore clustering, while intermetallic phases segregated at grain boundaries and influenced pore morphology. Results reveal that porosity is influenced not only by processing parameters but also by the interaction between alloy composition and secondary phases. Hence, optimizing processing parameters and phase distribution are critical to control defects and enhance the structural properties of aluminum alloy.

Acknowledgements

I would like to thank Professor Alberta Aversa for her guidance and collaboration throughout the development of this thesis. My sincere thanks go to Michele Rosito for his advice, patience, and assistance during my research journey. I also thank all the people I met in the DISAT laboratories, who helped me with the use of scientific instrumentation.

I would like to express my heartfelt gratitude to my mother, who has always supported me unconditionally, and to my father, whose guidance played a decisive role in my choice of the engineering profession. I am equally thankful to my beloved sisters and brother, who have been a constant source of joy and inspiration in my life. Above all, I am deeply indebted to them for their unwavering support in every respect, both materially and emotionally, throughout the journey. I am truly fortunate to have such supportive friends and colleagues. I have shared countless sweet and bitter memories with them, all of which made this adventure both meaningful and enjoyable. I am grateful to anyone who stood by my side. I am fully aware that without them, I would not have been able to overcome all the challenges on my own.

As a final note, this master's chapter has been far more than an academic experience; it has also been a personal path of growth, making me realize the importance of patience, resilience, and perseverance.

Esra AKILLI

Table of Contents

Table of Figures

Tables

1 Introduction

1.1 Background of Additive Manufacturing

Additive Manufacturing (AM) is a relatively new technology compared to the conventional machining processes of turning, milling, fabrication, and casting. Basically, the concept of producing a 3D object is layer by layer. Although there was a lot of research in the 1950s and 1960s, the remarkable developments were realized even early 1980s.

Its conception took place in 1984 with the invention of Stereolithography (SLA), which uses a laser to solidify a photo-sensitive liquid polymer. It was one of the first types of AM. [1] Charles Hull of UVP, Inc. (San Gabriel, California) described a process of directing a computer-controlled UV laser beam in a vat of photopolymer resin: 3D prototypes were formed by curing the resin layer by layer while submerging the build platform deeper into the vat. During this decade, AM technologies were mainly applied for rapid prototyping, focusing on design validation rather than end-use production. [2]

By the 1990s, with the introduction of metals into the world of Additive Manufacturing (AM), the scope of applications significantly diversified. AM processes began to be used for producing custom and flexible tooling, tooling inserts, jigs, and fixtures. Consequently, the term Rapid Tooling emerged to describe these specific applications.

Starting from the 2000s, recognizing the advantages of AM, several companies began investing in the enhancement of existing techniques and the development of novel technologies aimed at producing end-use parts through metal-AM. [3] In parallel, the world witnessed an exponential increase in the computing power of processors.

This technological advancement shifted component modelling from traditional 2D hand drafting to 3D Computer-Aided Design (CAD), which paved the way for the evolution of various metal-AM technologies. This transition also provided design engineers with an additional degree of freedom to transform their concepts into reality. [4] Specifically, in 2020, additive manufacturing became popular due to the COVID-19 pandemic, which allowed for the production of quick and cost-effective instruments.

The additive manufacturing workflow initiates with the detailed CAD model, which precisely defines the external and internal geometries of the component. This digital model is converted into a machine-readable format (e.g., STL), and then it is sliced into discrete layers to regulate the layer-by-layer deposition process. Subsequently, the machine setup is performed according to the requirements of the material system. Then, the part is printed. At the end of the printing process, the part is removed from the build platform and undergoes finishing operations. Since some of them require post-processing, such as thermal processing or surface finishing, to meet geometric tolerances and functional criteria. After the heat treatment, an inspection is carried out to prepare for finalization. The data flow is demonstrated in Figure 1.1

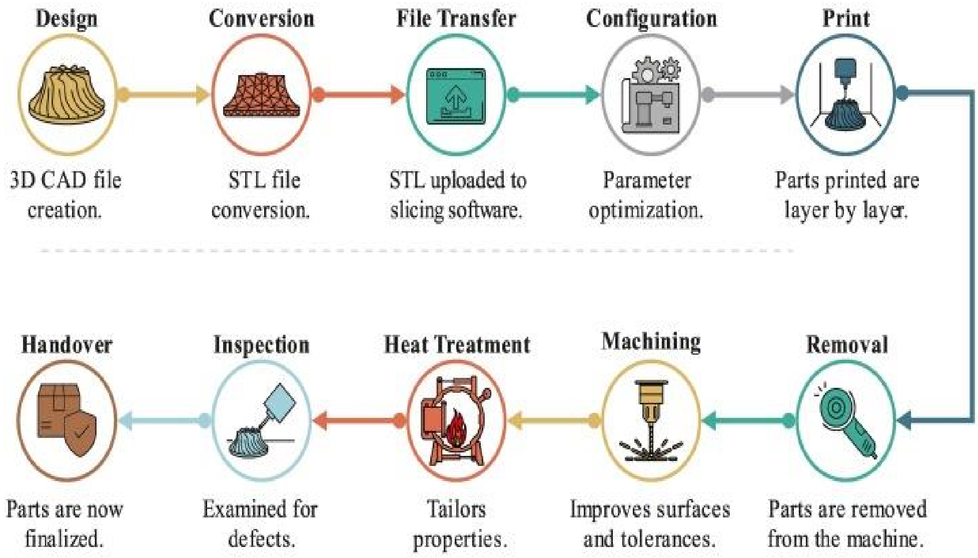

Figure 1.1: Data flow in AM [5]

The principles of Industry 4.0, including information transparency and decentralized machine decision-making, are more easily realized through Additive Manufacturing than with other conventional techniques, positioning AM as a major contributor to the new industrial paradigm.

1.2 Advantages of AM over traditional methods

One of the most significant advantages of Additive Manufacturing over traditional methods is the ability to produce highly complex components with great flexibility. In subtractive manufacturing, cutting tools are physically unable to access and create internal cavities. While formative methods like casting can create hollow features using cores, they are still limited in complexity. On the other hand, the AM methods enable the fabrication of complex internal geometries, including detailed lattice structures, which are extremely difficult to produce using conventional methods. Such lattice-based components often exhibit a better strength-to-weight ratio compared to their fully solid counterparts, mainly due to their ability to efficiently handle external loads and ensure uniform stress distribution throughout the part. [6]

AM also leads to flexibility in changing the designs of tooling, and this implementation allows for easy customization without the need for expensive tooling changes. In addition, AM enables on-demand manufacturing, which minimizes inventory costs. Around 60% of design changes occur during the production of tools, which requires significant costs and time. It also supports remote and distributed manufacturing, which is increasingly relevant in defense and aerospace applications. Traditional methods such as milling, turning, or drilling remove excess material, which often results in significant amounts of material waste. AM builds only what's needed, hence this minimizes waste significantly. [7] Incidentally, any unused powder in many AM systems can often be recycled and reused, further enhancing material efficiency and sustainability.

In Figure 1.2, the main part is about the convenience for a company in using an additive over a conventional process, then is finding the break-even point of the cost/piece geometric complexity graph. [8]

The graph demonstrates that for simple parts, traditional manufacturing has a lower cost; however, as geometric complexity increases, the traditional methods rise rapidly. In the AM process, the prices almost do not all impact. Furthermore, the traditional processes generally require complex tooling and molds; AM eliminates some tools, specifically in low-volume production or prototyping. Consequently, modern methods can offer ease for designers because of using a small fraction of the company's time and resources

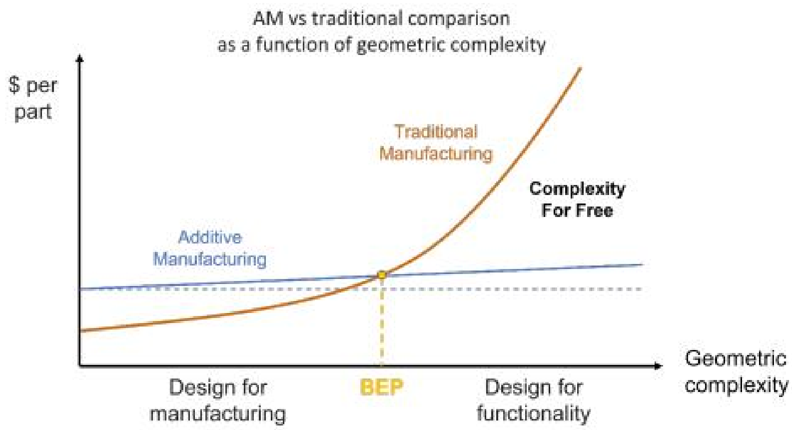

Figure 1.2: Comparison between AM and Traditional manufacturing [8]

The application of Additive Manufacturing in rapid prototyping significantly reduces lead times, as it eliminates time-consuming tooling modifications. Although in traditional methods, a complete redesign and fabrication of a new die is a requirement, with AM, design alterations can be implemented by adjusting the CAD model. Thanks to AM, it provides lightweight structures that are not achievable through traditional manufacturing approaches; therefore, this enables aerospace engineers can produce designed parts with topology-optimized components.

1.3 Limitations of AM

First and foremost, the range of materials that are used by traditional methods is wider than AM methods. Generally, layered manufacturing allows limited materials, for instance, some polymers, metals, or ceramics, owing to the fact that during the AM process, parameters such as metal powder preparation, filamentation, and sintering are not suitable for all materials. In addition, in some processes, the materials are not self-supporting, which creates the need for supports. Moreover, the poor surface finish of AM parts requires an additional stage of post-processing by traditional techniques. Hence, it causes extra time and resources. [8] This is mainly due to the layer-by-layer production process, which may result in surface roughness or visible lines on especially curved surfaces. Additionally, most AM technologies struggle with tight dimensional tolerances.

The AM has advantages for low and medium-volume productions; however, it has limitations in terms of high-volume products. In fact, traditional techniques require more lead-time; when the quantity of products to be manufactured is high enough, their production through traditional methods is generally faster with respect to the time required for processing the same number of components by AM techniques.

Porosity can be found within AM components due to the complex consolidation phenomena. The pores negatively impact the physical properties of the material, including yield strength, ultimate tensile strength, and elongation at break. Specifically, the irregular distribution of pores causes anisotropic material behaviors. The anisotropy stemming from different directions produces regions with varying mechanical strengths.

1.4 Classification of AM Processes

Generally, AM has seven different categories as demonstrated in Figure 1.3: Directed Energy Deposition (DED), Binder Jetting (BJ), Material Extrusion (MEX), Material Jetting (MJT), Powder Bed Fusion (PBF), Sheet Lamination (SHL), and VAT Photopolymerization (VPP). [9]

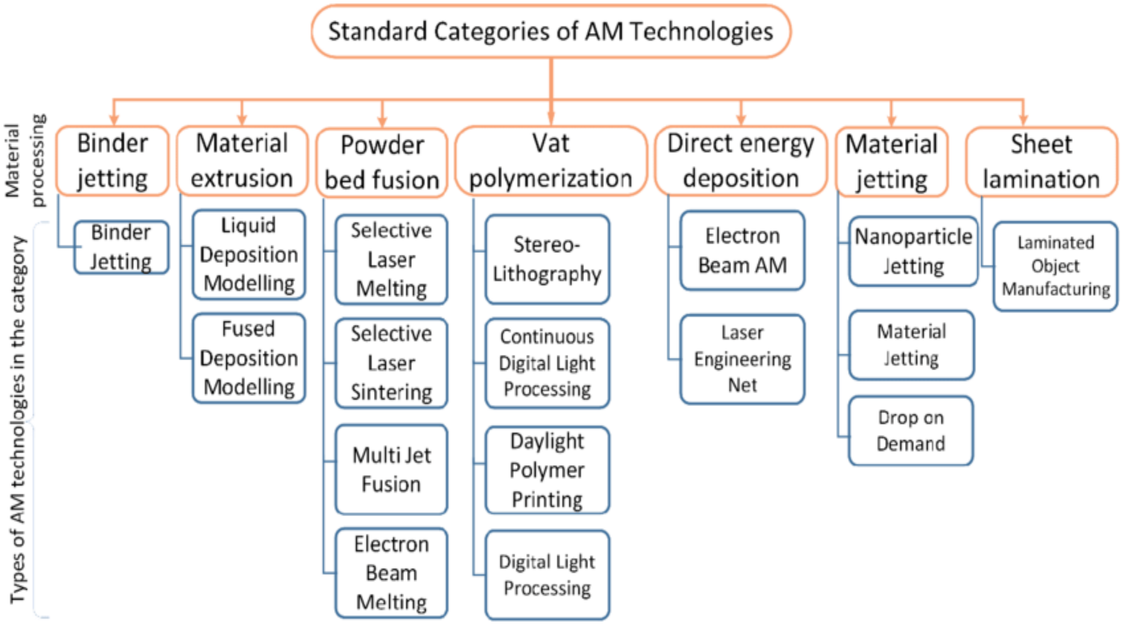

Figure 1.3 Additive Manufacturing Types [9]

In the Binder Jetting (BJ) process (Figure 1.4), a liquid binding agent is selectively deposited onto a thin layer of powder material, bonding the powder particles together to form a solid part layer by layer. Initially, a thin layer of powder is applied on the build platform, followed by an inkjet printhead that moves over the powder bed. After one layer is completed, the build platform lowers, and a new layer of powder is spread on top. The steps are repeated until the complete part is formed. [10]

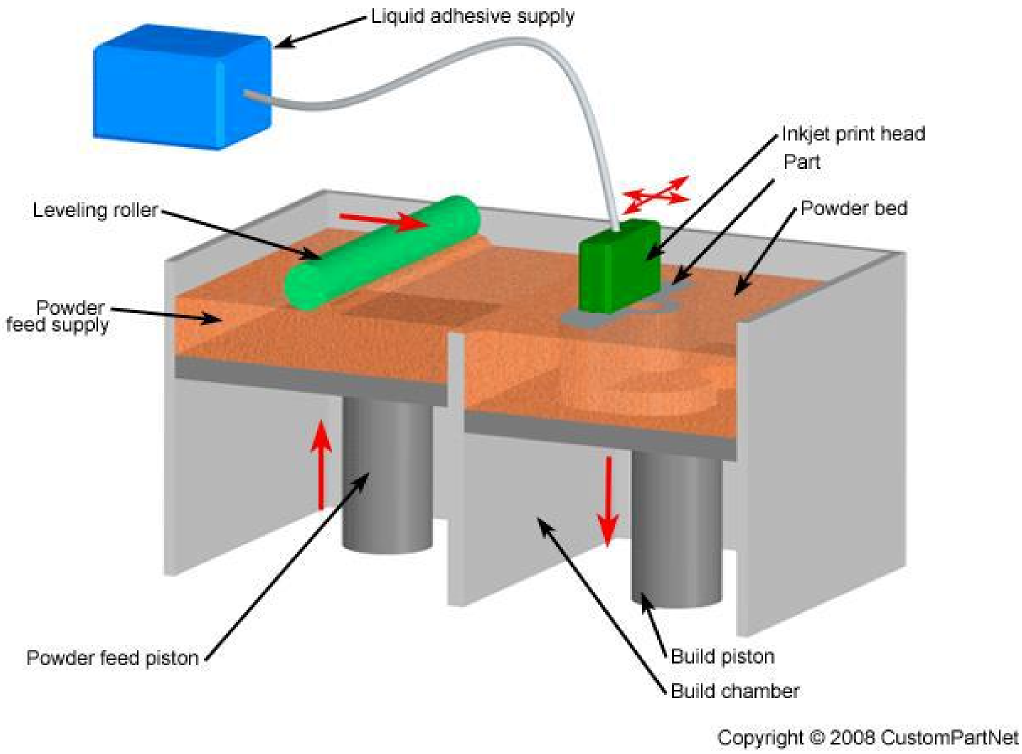

Figure 1.4 Binder Jetting mechanism [11]

Powder bed fusion has the advantage that the energy to melt or sinter the material is powdered (Figure 1.5). The powdered material is a form of bed that is heated to its melting point, stopping below the precise temperature. After, the source of the energy is given to the surface in order to bond the material to form a layer. The PBF process is usually conducted in a vacuum chamber to prevent the material from corrosion. In the material extrusion process (Figure 1.6), a part is produced by extruding molten material, usually thermoplastic or composite, through a nozzle. For example, fused deposition modelling is a common technology. This method is easily accessible and suitable for rapid prototyping [12].

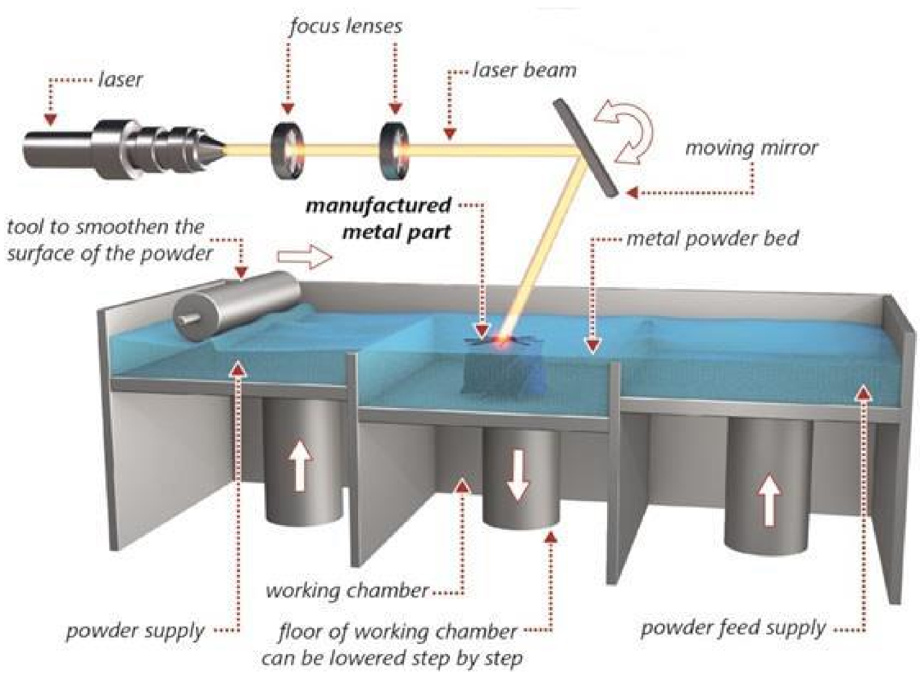

Figure 1.5 Powder bed fusion machine specific for metals [13]

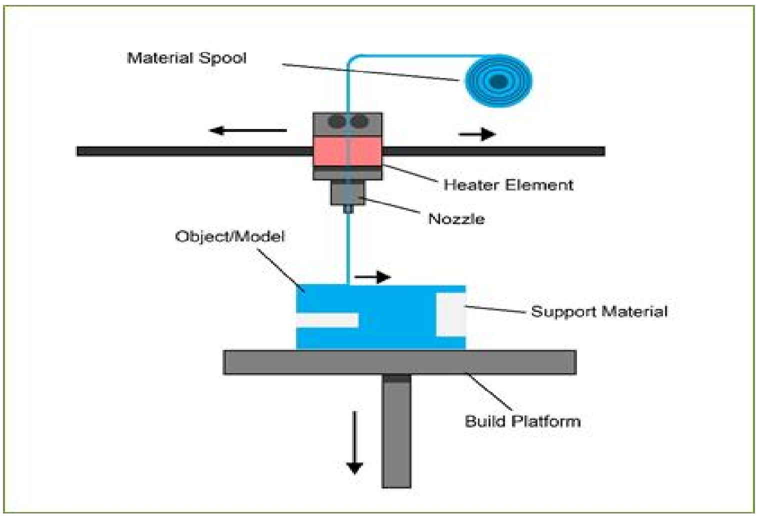

Figure 1.6 Material extrusion (MEX) process [14]

Production by curing liquid resin layer by layer using UV or another light source in VAT polymerization. This method is typical of the Stereolithography process. The principle is the same for mask projection and two photons in the sense that a photo-sensitive resin solidifies, as well as ensuring extremely high surface quality and resolution.

Material Jetting (MJT) production is similar to inkjet printing documents, but instead of printing ink drops on paper, building material is dropped onto the build platform using either a continuous or drop-on-demand approach, which can provide multi-color printing [15].

Sheet lamination (SHL) is produced by bonding or soldering thin sheets of metal or other materials. This method wastes less material and manufactures at high speeds, but geometric complexity is limited.

The Directed Energy Deposition (DED) process is clarified with details in Chapter 3.

2. A2618+Ti+B Properties

2.1 Composition and Microstructure

The base alloy A2618 consists primarily of the Al-Cu-Mg-Fe-Ni system and is generally designed for high-temperature aerospace applications. Its chemical composition is as follows in Table 2.1. According to the graph, the elements' functions in the alloy system respectively: aluminum is mainly the matrix phase, providing ductility; copper is precipitation hardening, and θ-phase (Al_2Cu) during artificial aging, raising yield strength and hardness. Magnesium is a solid solution strengthening that contributes to the Al_2CuMg phase.

Table 2.1 Composition of the A2618 [16]

Elements	**Composition (%)**
Aluminum (Al)	Balance
Copper (Cu)	2.0 – 2.8
Iron (Fe)	1.0 – 1.4
Nickel (Ni)	1.0 – 1.8
Magnesium (Mg)	1.2 – 1.8
Silicon (Si)	0.1 – 0.25
Titanium (Ti)	0.04 – 0.15
Other Elements	≤ 0.15

Iron forms Al_7Cu_2Fe intermetallic increases creep resistance, improving high temperature stability. Nickel can enhance creep resistance and stabilize intermetallic phases. Although silicon contents are lower than 0.25 wt%, they minimize solidification shrinkages [16]. Ti and B additions to A2618 act as a grain refiner via TiB_2 formation. Titanium (Ti) reacts with boron to produce fine, stable TiB_2 ceramic particles that are thermodynamically stable and chemically inert, ensuring they remain unaltered during the AM processing. These particles behave as heterogeneous nucleation sites, leading to fine-grained structures. Therefore, the refinement of grain structure improves both isotropy and mechanical performance, for example, increased yield strength, fatigue, and wear resistance and reduces anisotropy defects. Ti + B into A2618 alloy transforms its microstructure into a hybrid metal matrix composite, the ductility of the aluminum matrix, the strengthening effect of intermetallic phases, and the hardness stability of TiB_2 ceramics.

This unique composition makes A2618+Ti+B particularly suitable for lightweight, high-strength, high-temperature aerospace components where wear resistance and structural integrity are critical [17].

The base microstructure of this alloy exhibits;

α-Al primary phase: the aluminum-rich phase that forms the continuous matrix as providing ductility and toughness thanks to its face-centered cubic (FCC) crystal structure. In addition, the phase ensures corrosion resistance as aluminum forms a stable oxide layer [18]. Intermetallic Phases: several intermetallic compounds through precipitate during solidification and heat treatment. Their morphology, distribution, and volume fraction critically determine strength, creep resistance, and fatigue behavior.

θ-phase (Al_2Cu): the function is mainly strengthening via precipitation hardening, as well as hindering dislocation motion, thus increasing yield strength and hardness. However, over-aging can lead to coarsening, reducing effectiveness.

Especially in aerospace applications, the θ-phase requires careful thermal management to maintain performance. Coarse or discontinuous θ-phase particles, particularly along the grain boundaries, can act as stress concentrators, potentially crack initiation under cyclic or impact loading [18,19,20]

S-phase (Al_2CuMg): It forms in Cu-Mg-rich regions and is frequently observed along the grain boundaries, depending on the heat treatment parameters. It contributes to increased strength and wear resistance. The S-phase plays a significant role in enhancing the mechanical performance of A2618 alloy. While its thermal stability is slightly inferior to that of the **θ-phase phase** it remains beneficial for applications operating at room temperature to intermediate temperature (150-200 °C) [20].

Ni-containing phases (Al_3Ni, Al_2CuNi): Firstly, nickel has low solubility (less than 0.04 wt% at the eutectic temperature), which promotes the phenomenon of thermally stable intermetallic compounds during solidification. In A2618 and similar Ni-containing aluminum alloys, the most common intermetallics are Al_3Ni, is often forms during primary solidification or through eutectic reactions. Al_2CuNi forms when both Ni and Cu are present in adequate amounts during the final stages of solidification. These phases are stable during casting and high-temperature service owing to the fact that Ni's low diffusivity in the aluminum matrix, which implies that they resist coarsening during prolonged thermal exposure. These factors are critical in terms of aerospace components operating under temperatures (200-300°C). The function and role of Al_3Ni and Al_2CuNi in properties significantly enhance the creep resistance. Their stability ensures that the strengthening effects are preserved after long thermal exposure. Moreover, they enhance low-cycle fatigue resistance under thermal cycling conditions. Their morphology and dispersion are critical and uniform; fine distribution yields better mechanical performance, whereas segregation can act as a crack initiation.

Fe-rich phases (Al_7Cu_2Fe): Fe-rich intermetallic compounds such as Al_7Cu_2Fe typically form in aluminum alloys due to the presence of iron, which is often introduced as an impurity during melting and alloy preparation. Iron is difficult to eliminate due to it is strong enough to form intermetallic phases.

These phases precipitate during the solidification stage of casting and are thermodynamically stable within the aluminum matrix. Its major function and effects in sequence, Fe-rich intermetallic Al_7Cu_2Fe exhibit high thermal stability, maintaining their structure even at elevated temperatures. Despite their stability, these Fe-rich phases frequently form coarse and brittle particles within the microstructure. Their brittleness is a result of the complex crystal structure and inherent hardness of the intermetallic compound.These coarse particles can operate as stress concentrators, notably under mechanical loading or thermal cycling conditions. Consequently, they are potential sites for crack initiation and propagation, which can reduce the fatigue and toughness of the part. The microstructural control is required in order to diminish the negative impacts of Fe-rich phases. Optimizing solidification rates can be applied through faster cooling, which can lower the size and coarseness of these intermetallics, improving mechanical properties.

The roles of Ti and B (TiB_2) in microstructure modification, as microalloying elements, are a common practice to refine the grain structure and enhance mechanical properties through the formation of nucleating particles. Ti and B as potential grain refiners, especially during the solidification, promote the formation of TiB_2 particles, which serve as heterogeneous nucleation sites for α-Al grains. Therefore, it occurs in a finer and much uniform grain structure that is crucial in developing the strength, toughness, and fatigue resistance of the material. Besides, finer grains can minimize hot cracking susceptibility during the processing, such as Directed Energy Deposition or casting [21]. The refined microstructure achieved by Ti + B additions increases yield strength and ultimate tensile strength via the grain boundary (Hall-Petch effect).

As a further point, a more uniform grain size distribution results in improved ductility and resistance to crack initiation, which is essential for aerospace components. Besides, TiB_2 particles may contribute to dispersion strengthening, where hard particles hinder dislocation [22]. Ti and B additions can influence the morphology and distribution of intermetallic phases within the matrix. The θ-phase and S-phase, which are the dispersed precipitates, are created by the refined grain, improving age hardening and thermal stability.

The necessity to control the size and distribution of these phases minimizes the localized stress concentrations and boosts fatigue characteristics. In the directed energy deposition processes, particles from Ti and B additions assist in stabilizing the melt pool dynamics and reducing solidification defects, such as porosity and hot cracking [23].

Accordingly, these significantly alter its microstructures by promoting grain refinement. These additions are beneficial in terms of additive manufacturing processes in DED, where controlling microstructural features is requisite for producing high-performance aerospace components.

2.2 Mechanical Properties

The aspects of mechanical properties, in studies adding TiB_2, resulted in remarkable improvements: tensile strength increased by approximately 25-26 %, values typically in the range of 430 – 460 MPa. yield strength demonstrated around 29%, and Brinell hardness rose to 43%. Optimal mechanical performance is observed at around 3 wt% TiB_2, both strengthening and ductility, for example, elongation 9.8%. The fatigue life is extended due to the reduced grain size and improved microstructural stability at elevated temperatures, and creep resistance benefits from thermally stable Ni- containing intermetallics.

It is shown in Table 2.2 All of these developments arise from grain refinement strengthening (Hall-Petch effect), Orowan strengthening is where hard particles hinder dislocation, and load-bearing contribution from rigid TiB_2 particles [24].

Table 2.2 Effect of Ti and B addition to A2618's mechanical properties [25]

Property	**Estimated Enhancement with** TiB_2
Tensile Strength	20 – 30 %
Yield Strength	25 – 35 %
Hardness (Brinell)	30 – 40 %
Elongation	Maintained (approx 9 – 10 %)
Fatigue&Creep Resistance	Improved (finer microstructure)

TiB_2 functions as an abrasion-resistant, enhancing surface endurance in friction or mechanical wear conditions, an important phenomenon for aerospace sectors where these parts are in relative motion [26].

3. Directed Energy Deposition (DED) Process

3.1 Process Overview

Directed Energy Deposition (DED) is an additive manufacturing technique that utilizes focused thermal energy to simultaneously melt and deposit material onto a substrate during the fabrication process. Figure 3.1 indicates the working of DED. A laser beam is focused on the substrate. The substrate can be different depending on the purpose of using DED.

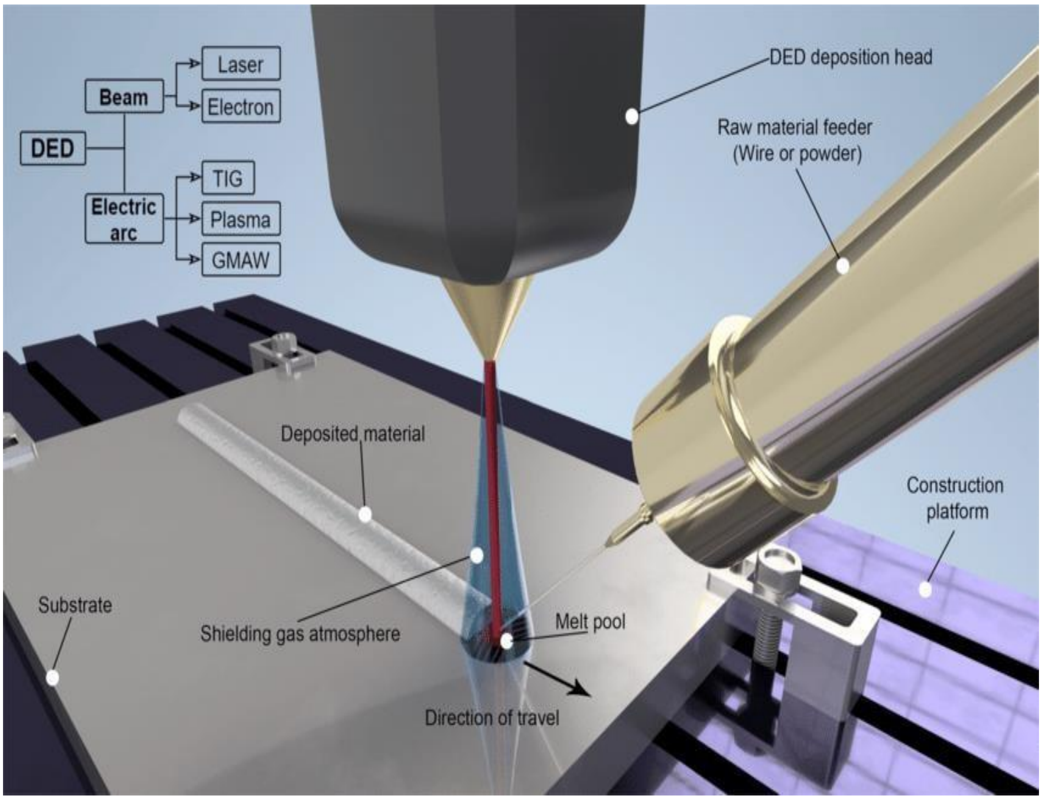

Figure 3.1 DED illustration [27]

It can be a metal plate for building a new component, or it can be a component that is to be repaired or coated [27]. DED creates parts by melting and depositing material at the same time, from thin wire or powder feedstock, and the focused heat source can be an electron beam or a laser beam in Figure 3.2

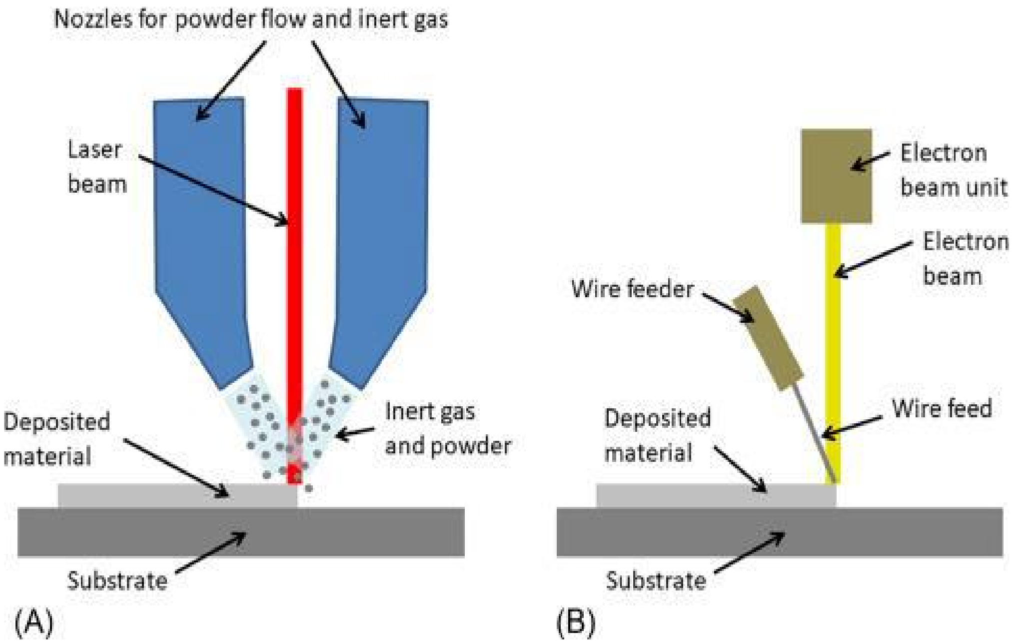

Figure 3.2 (a) laser beam and powder feedstock (b) electron beam and wire [28]

Wire feedstock implies a deposition efficiency of nearly 100%, as almost all the material used is melted and deposited onto the substrate [28]. Powder, instead, is a more versatile feedstock, which can be used to build more complex objects, particularly if they have thick and thin regions. The electron beam system is used within a vacuum chamber and often does not encounter main oxidation issues. However, laser systems require specific methods to oxidation under control. The most common configuration is laser (L-DED) using powder feedstock. Additionally, the laser beam used in the region of the melt pool is shielded with an inert gas, usually argon, to prevent oxidation of the melted metal [29]. In summary, during the process, the laser melts small point of the substrate, producing the melt pool, shown in Figure 3.3

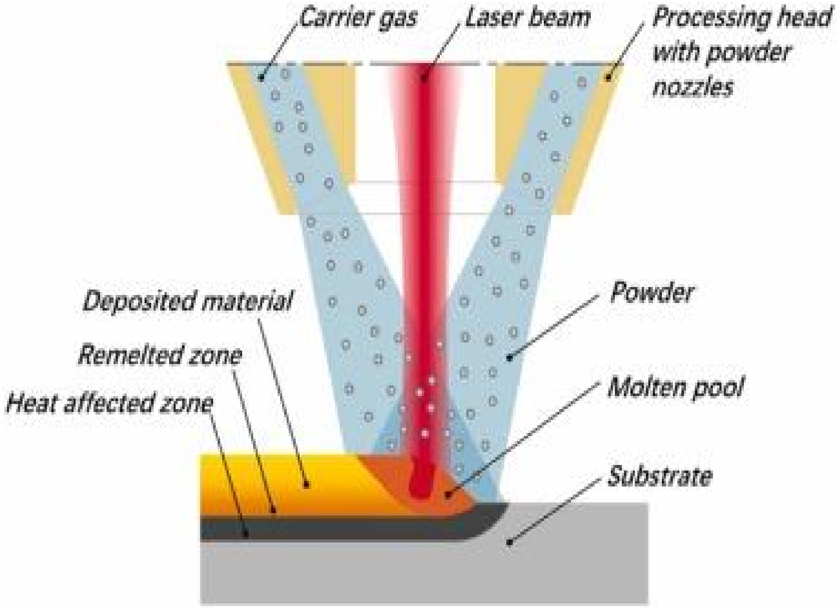

Figure 3.3 Melt pool in DED [30]

A powder is deposited into the melt pool, it melts and solidifies as soon as the laser beam moves away, occurring a thin track. Its dimensions depend on some factors like the material and laser characteristics. Considering the short period of the melting process, the high cooling rates (1000-5000 K/s) are frequently used, producing large thermal gradients and non-equilibrium grain structures, which cannot be achieved by traditional manufacturing ways, like as casting. Tracks overlap by approximately 25% of their width, creating layers. These overlaps cause the previously deposited material to re-melt. [30] Through nozzles, transport and eject powder particles by an inert gas carrier, such as nitrogen or argon. It can be seen in Figure 3.4, various common nozzle configurations.

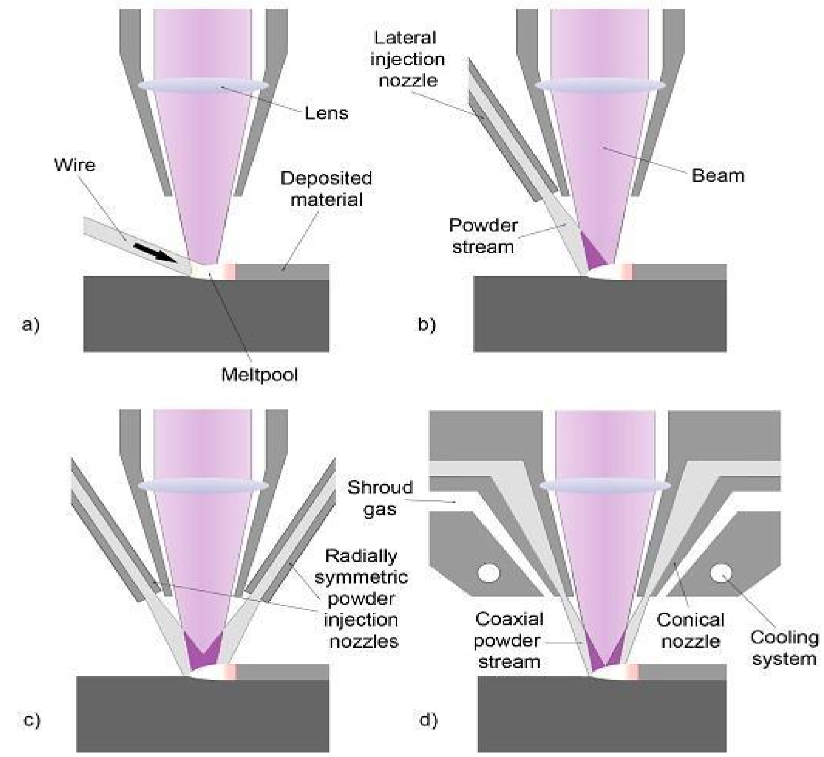

Figure 3.4 Different nozzle configurations. a) wire, b) single lateral nozzle, c) radially symmetric nozzles, and d) conical nozzle [31]

In summary, DED a powder is deposited into the melt pool, it melts and solidifies as soon as the laser beam moves away, occurring a thin track. Its dimensions depend on some factors, like the material and laser characteristics.

3.2 Advantages and Drawbacks of DED

DED is a rather new technology, and there are some advantages and disadvantages compared to conventional manufacturing methods.

The principal advantages are, sequentially,

- **Design flexibility and complex geometry of productions**: DED allows the creation of complex and customized geometries. This is particularly advantageous in prototyping, repair, and low-volume production. Furthermore, existing parts can be repaired and indicating that hybrid manufacturing [32].

- **High deposition rate and productivity**: DED generally has higher material deposition rates than other AM methods, therefore minimizing part production period and increasing production efficiency. Specifically, this is useful when manufacturing large-sized or thick parts.

- **Material versatility**: The DED process uses various materials like metal, ceramic, and composite. Besides, it can be realized that integrating with different materials in regions or layers within the same part and the key benefit can offer optimization of functional and mechanical properties [33].

- **Minimum material waste:** is provided because the fact that material is used only in areas where it is needed, and waste is significantly low. This is a significant economic and environmental advantage [32,33].

DED is not advantageous under all conditions and may include some disadvantages.

- **Surface finish**: typically after the printing step, parts require post-processing such as machining or grinding, and reaching tight tolerances can be difficult without secondary finishing steps .

- **Thermal distortion and residual stresses**: the localized high energy can cause distortion or microstructural heterogeneity, and therefore, after the deposition, may require stress-relief heat treatments.

- **Equipment and operational costs**: specifically, initial investments, machines or equipment prices are expensive, for instance, electron beam DED needs a vacuum chamber, or laser DED needs inert shielding [32].

The parameters are sensitive during the manufacturing; precise control is necessary, such as beam power, powder feed rate, and shielding gas flow. Additionally, the DED machine setup adjustments are complex. Operators must be well-skilled.

3.3 Characteristic parameters of laser-powder DED

In the manufacturing of directed energy deposition stages, process parameters have a vital influence on the quality of products. They can be mainly divided into the following categories:

- **Laser Power (P):** Its definition is the energy output of the laser. It has an impact on the melt pool size in terms of penetration and deposition rate. However, high power can cause over-melting and evaporation of alloying elements. Operators should be careful about optimization between enough melting and distortion [34].

- **Scanning Speed (v)**: It refers to the laser's movement speed. This parameter is between the laser and the material. Controlling heat input per unit length, low scanning speed means that higher heat input. However, high speed results in finer grains and incomplete melting areas.

- **Linear Energy Density (LED, J/mm)**: In directed energy density (DED), LED refers to the amount of laser energy supplied per unit length of the deposition path, which determines how much energy is delivered to the substrate or powder per millimeter of scanning distance [35]

The formulation of the LED is;

$$\text{LED (J / mm)} = \frac{P}{v}$$

P = Laser Power (W = J / s)

v = Scanning Speed (mm/s)

Low LED leads to insufficient energy and poor metallurgical bonding among layers. On the other hand, excessive melting and dilution, or residual stress, occur in high LED; thus, an optimal LED is necessary to provide balance.

- **Z step:** It is the incremental build height refers to the vertical displacement of the deposition build platform after each layer is completed. Unit is millimeters (mm), typical values and applications of Z as thin layers and thick layers.

- **Laser Spot Size**: refers to the diameter of the laser beam at the point where it hits the substrate or powder.

- **Powder Feed Rate**: It means that the mass flow of powder into the melt pool, if it is too high, it causes unmelted powder, porosity. However, it is too low; it may result in discontinuous tracks.

4. Materials and Methods

4.1 Flowability Measurement

The flowability of metallic powders is a crucial parameter in additive manufacturing, as it directly affects layer uniformity and density during the powder process. Flowability is typically measured using a standard Hall flowmeter funnel (Figure 5.1), where the time required for a fixed mass of powder to pass through a calibrated orifice is measured [36].

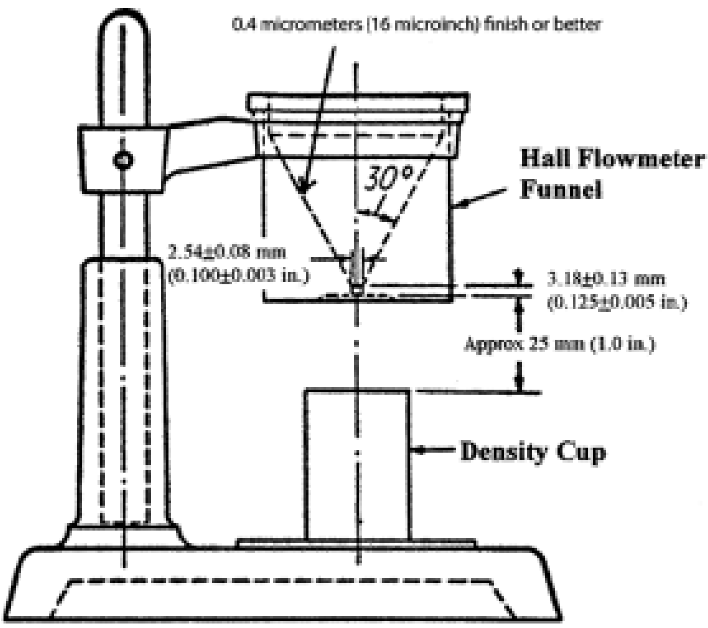

Figure 4.1 Hall Flowmeter Apparatus [37]

The procedure to measure the flowability using the Hall Flowmeter is defined in ASTM B213-13 standard, which follows:

1) 50 grams of powder is weighed and placed into a container.
2) The powder is poured into the funnel of the Hall flowmeter. It should be noted that the finger is dry because the orifice is blocked by the bottom of the funnel with a finger.
3) Another container is placed at the bottom of the funnel to collect the powder that falls from the cone.
4) The orifice is unblocked by removing the finger, allowing the powder to flow freely into the container below. Time measurement should start simultaneously with the orifice being unblocked.
5) The time measurement is over when the last particle of powder falls into the container below the funnel

The procedure measures the time required for 50 grams of powder to pass through the funnel, taking into account sensitivities to moisture, electrostatic charge, and handling method [38].

4.2 Density Measurement

4.2.1 Apparent Density

This test method provides a guide for the evaluation of the physical characteristic of a powder known as the apparent density. The measured apparent density corresponds to the amount of powder that occupies a die cavity of fixed volume.

The level of correlation between the results of this test and the performance of powders in use variety of particular applications. However, the presence of moisture, oils, stearic acid, stearates, and the temperature of the powder mass may change the physical characteristics of powders. In other words, apparent density is the mass of a given volume of loose (untapped) powder, including the spaces between particles, except for applying any external pressure or vibration.

Brief of the testing method: a volume of powder is permitted to flow into a container of definite volume under controlled conditions. The mass of powder per unit volume is determined as apparent density [39].

Calculate the apparent density with this formula:

$$Apparent\ Density = \frac{Mass\ of\ powder\ (g)}{Volume\ Occupied\ (cm^3)}$$

4.2.2 Tapped Density

Tapped density is the density obtained by a powder after compaction, when the particles must settle to a fixed volume in a defined position. The process to measure the quantity has been carried out with the described methods in the following paragraph.

1. Cleaning the inside of the cylinder tube (Figure 4.2) with solvent or alcohol, then thoroughly drying it previous reusing it.
2. Weighed the mass of the test portion as indicated in the table
3. The cylinder is filled with powder. Please take care of the level of the powder.
4. The system is swashed that the powder inside the cylinder gets compacted and space is created inside.

The obtained values of masses are then used to calculate the tapped density in this formula:

$$\rho_{tapped} = \frac{m_{tapped}}{V}$$

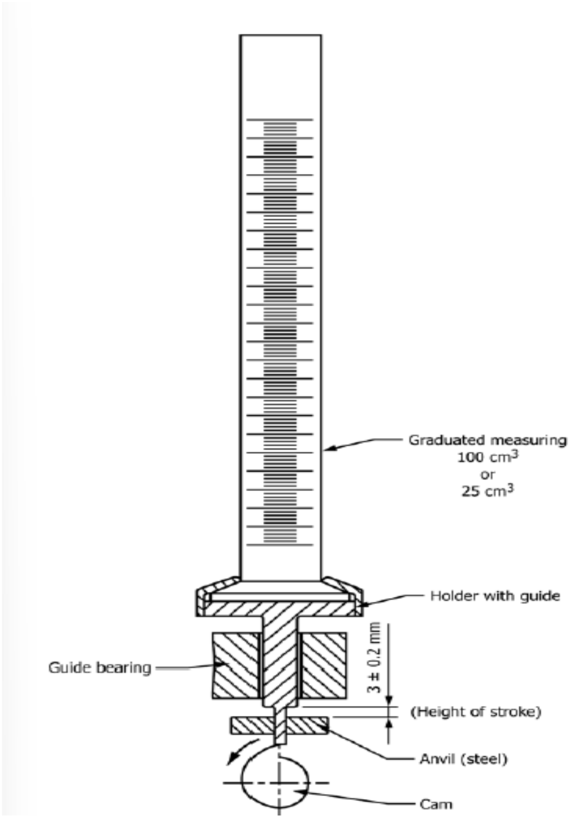

Figure 4.2 Tapping Apparatus [40]

Where m_{tapped} is the average of the masses of powder obtained at the end of the test,
V: Internal volume of cylinder (cm^3)

A different form of density is bulk density, which means that the mass of powder per unit volume, including the void spaces between particles [41].

$$\rho_{bulk} = \frac{m_{bulk}}{V}$$

Where m_{bulk} is the average of the masses of powder obtained in step 3 (grams),
V: Internal volume of cylinder (cm^3)

These two values of ρ_{bulk} and ρ_{tapped} are used to calculate the compressibility Index as follows:

$$Compressibility\ Index = \left(\frac{\rho_{tapped} - \rho_{bulk}}{\rho_{tapped}}\right) \text{ x } 100$$

The obtained values from the compressibility Index demonstrate the flowability of the powder in Table 4.1.

Table 4.1 Flowability characteristics of powder [42]

Compressibility Index (%)	**Flow Character**
<10	Excellent
11-15	Good
16-20	Fair
21-25	Passable
26-31	Poor
30-37	Very Poor
>38	Very very poor

4.3 Samples Production and Characterization

Thin-wall samples were built using a BeAM Modulo 400 DED system, a 5-axis gantry machine. The process was performed in a fully argon atmosphere inside the chamber (below 100 ppm O_2) and powder carrier gas rate 5 L/min, secondary gas 10 L/min, and central gas 6 L/min (also argon). Below is Figure 4.3, the illustration of the samples that were made in the study.

ID	P [W]	v [mm/s]	LED (J/mm)	Δz [mm]	Layer [No.]	Cracked
1	1000	1000	1	0.66	20	
2	1200	1000	1,2	0.66	20	
3	1400	1000	1,4	0.66	20	
4	1600	1000	1,6	0.66	20	
5	1800	1000	1,8	0.66	20	
6	1000	1200	0,8	0.66	20	Cracked
7	1200	1200	1,0	0.66	20	
8	1400	1200	1,2	0.66	20	
9	1600	1200	1,3	0.66	20	
10	1800	1200	1,5	0.66	20	
11	1000	1400	0,7	0.66	20	Cracked
12	1200	1400	0,9	0.66	20	
13	1400	1400	1,0	0.66	20	
14	1600	1400	1,1	0.66	20	
15	1800	1400	1,3	0.66	20	
16	1000	1600	0,6	0.66	20	Cracked
17	1200	1600	0,8	0.66	20	
18	1400	1600	0,9	0.66	20	
19	1600	1600	1,0	0.66	20	
20	1800	1600	1,1	0.66	20	
21	1000	1800	0,6	0.66	20	Cracked
22	1200	1800	0,7	0.66	20	
23	1400	1800	0,8	0.66	20	
24	1600	1800	0,9	0.66	20	
25	1800	1800	1,0	0.66	20	

Figure 4.3 samples with numbers

Samples are identified as numbers; the total samples are twenty-five. Figures 4.4 and 4.5 show three different aspects of the samples' photos as front, back, and top.

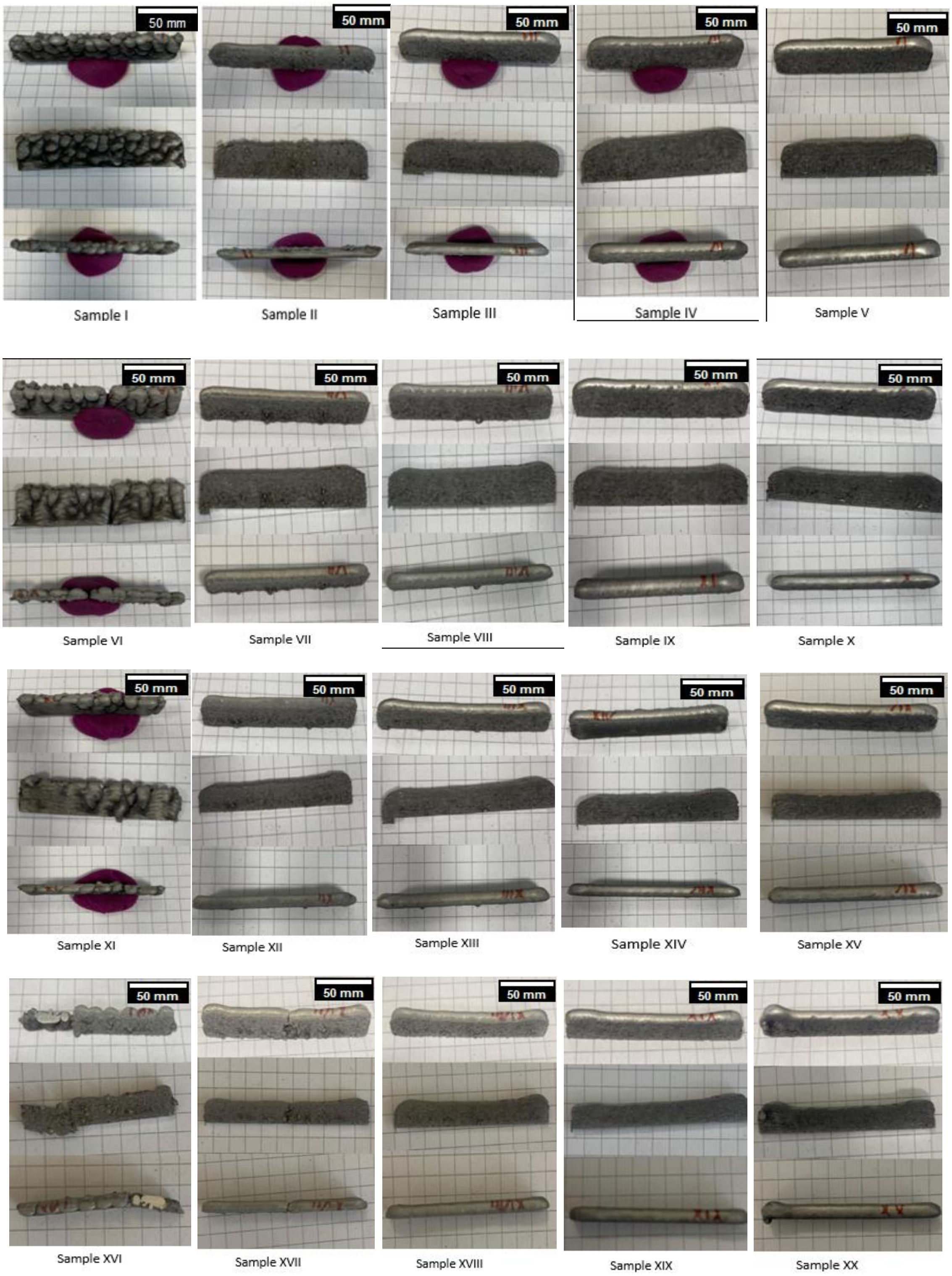

Figure 4.4: back-front-top photos of samples (1-20)

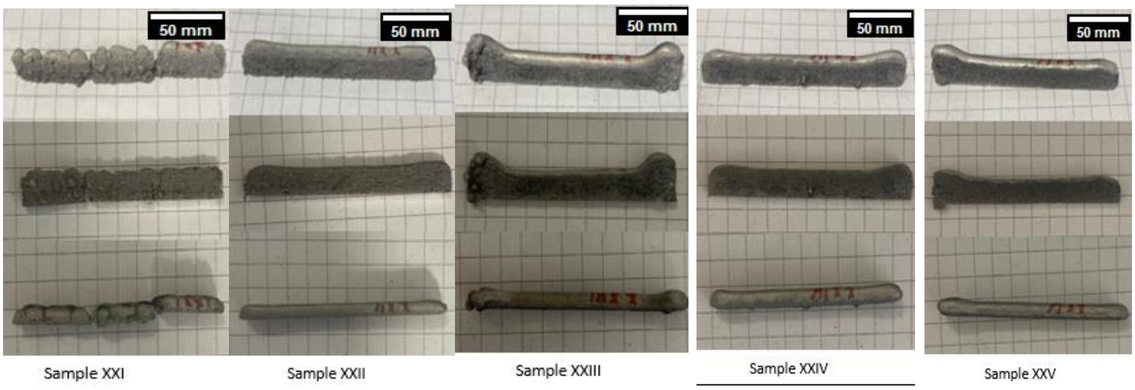

Figure 4.5: back-front-top photos of samples (21-25)

As we can see in Figure 4.3, the laser parameters and dimensions of samples, in addition, crack formation, have been observed in some samples that are labeled as ‘cracked’. The combination of low power, as 1000 W, and low LED (J/mm) makes it more prone to cracks. Furthermore, cracked samples (ID 6, 11, 16, 21) have the lowest LED values.

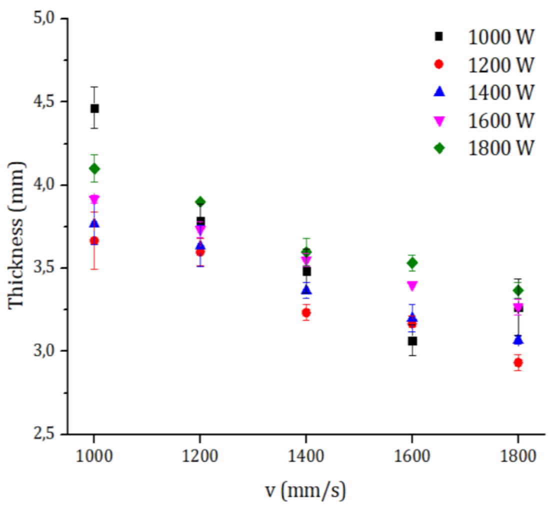

Figure 4.6: Sample Thickness with Scanning Speeds

ID	P [W]	v [mm/s]	LED (J/mm)	Thickness (different aspects mm)						
				Extremity Left	middle 1	middle 2	middle 3	Extremity Right	Average Thickness	SD Thickness
1	1000	1000	1	4,4	4,6	4,5	4,3	4,3	4,47	0,12
2	1200	1000	1,2	3,8	3,5	3,9	3,6	4,4	3,67	0,17
3	1400	1000	1,4	3,7	3,6	3,8	3,9	4	3,77	0,12
4	1600	1000	1,6	4,1	3,9	3,95	3,9	4,3	3,92	0,02
5	1800	1000	1,8	4,3	4	4,2	4,1	4,4	4,10	0,08
6	1000	1200	0,8	3,6	3,65	3,8	3,9	3,5	3,78	0,10
7	1200	1200	1,0	3,4	3,5	3,7	3,6	3,6	3,60	0,08
8	1400	1200	1,2	3,6	3,8	3,6	3,5	3,8	3,63	0,12
9	1600	1200	1,3	3,9	3,7	3,7	3,8	4	3,73	0,05
10	1800	1200	1,5	4,1	3,9	3,9	3,9	4	3,90	-
11	1000	1400	0,7	3,2	3,3	3,55	3,6	3,6	3,48	0,13
12	1200	1400	0,9	3,4	3,2	3,2	3,3	3,3	3,23	0,05
13	1400	1400	1,0	3,5	3,4	3,3	3,4	3,4	3,37	0,05
14	1600	1400	1,1	3,6	3,5	3,55	3,6	3,55	3,55	0,04
15	1800	1400	1,3	3,9	3,7	3,6	3,5	3,8	3,60	0,08
16	1000	1600	0,6	3,1	3	3,2	3	3,2	3,07	0,09
17	1200	1600	0,8	3,1	3,2	3,2	3,1	3	3,17	0,05
18	1400	1600	0,9	3,2	3,1	3,3	3,2	3,4	3,20	0,08
19	1600	1600	1,0	3,5	3,4	3,4	3,4	3,6	3,40	-
20	1800	1600	1,1	3,7	3,6	3,5	3,5	3,6	3,53	0,05
21	1000	1800	0,6	3	3,1	3,5	3,2	3	3,27	0,17
22	1200	1800	0,7	3	2,9	3	2,9	3	2,93	0,05
23	1400	1800	0,8	3,4	3,1	3,05	3,05	3,3	3,07	0,02
24	1600	1800	0,9	3,3	3,3	3,3	3,2	3,2	3,27	0,05
25	1800	1800	1,0	3,3	3,4	3,4	3,3	3,6	3,37	0,05

Figure 4.7:Thickness of samples

Sample thickness with its scanning speed value can be seen in Figure 4.6. At lower scanning speeds (1000-1200 mm/s), relatively higher thickness values are obtained due to prolonged laser material interaction. In contrast, as the scanning speed increased to 1600-1800 mm/s, the sample thickness decreased to approximately 3.0 – 3.3 mm. Generally, sample thickness decreases with increasing scanning speed, regardless of laser power. Figure 4.7 presents thickness measurements at different positions on the sample. Extremely left, middle 1, middle 2 (central positions), middle 3, and finally extremely right. Additionally, the table includes average thickness (mean of all measured thickness values), standard deviation (SD), and thickness (measures variation in thickness uniformity).

Consequently, thickness uniformity as standard deviation, lower SD values indicate better thickness uniformity. Figure 4.8 depicts that at a scanning speed of 1000 mm/s, the sample height ranged between 10 and 12 mm, with the maximum value observed at 1000 W. As the scanning speed increased, the sample height decreased, reaching 6-7 mm at 1800 mm/s. Moreover, at higher scanning speeds, the effects of laser power diminish. However, the effect of laser power is dominant at lower scanning speeds.

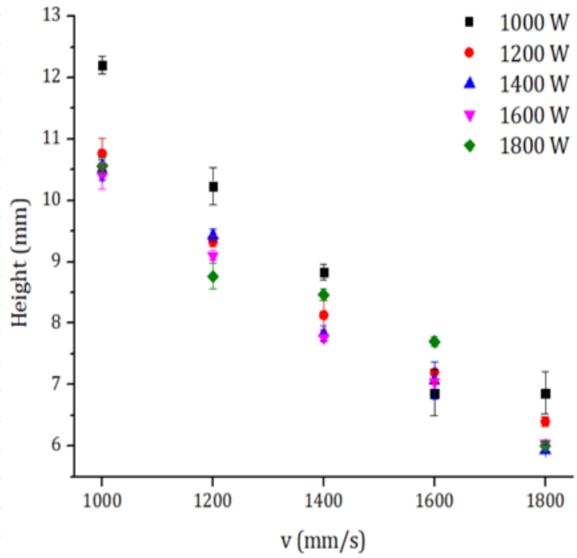

Figure 4.8 Height of samples with scanning speeds

ID	P [W]	v [mm/s]	LED (J/mm)	Height (different aspects mm)						
				Extremity Left	middle 1	middle 2	middle 3	Extremity Right	Average Height	SD Height
1	1000	1000	1	12,45	12,1	12,4	12,1	11,5	12,20	0,14
2	1200	1000	1,2	11,7	10,5	10,7	11,1	10,7	10,77	0,25
3	1400	1000	1,4	11,2	10,7	10,5	10,3	10,2	10,50	0,16
4	1600	1000	1,6	11,1	10,6	10,5	10,1	10,3	10,40	0,22
5	1800	1000	1,8	11,1	10,6	10,7	10,4	10,5	10,57	0,12
6	1000	1200	0,8	10,1	10,5	10,4	9,8	9,7	10,23	0,31
7	1200	1200	1,0	10,2	9,4	9,4	9,2	10,1	9,33	0,09
8	1400	1200	1,2	10,2	9,5	9,3	9,5	9,5	9,43	0,09
9	1600	1200	1,3	9,9	9,2	9	9,1	9,4	9,10	0,08
10	1800	1200	1,5	9,8	9	8,8	8,5	8,5	8,77	0,21
11	1000	1400	0,7	9,9	9	8,8	8,7	8,8	8,83	0,12
12	1200	1400	0,9	9,4	8,3	8,3	7,8	8	8,13	0,24
13	1400	1400	1,0	9	8	7,7	7,8	8,2	7,83	0,12
14	1600	1400	1,1	8,7	7,8	7,7	7,8	7,9	7,77	0,05
15	1800	1400	1,3	9,3	8,6	8,4	8,4	8,9	8,47	0,09
16	1000	1600	0,6	7,9	6,4	7,3	6,9	7,4	6,87	0,37
17	1200	1600	0,8	8,3	7,4	7,2	7	7,5	7,20	0,16
18	1400	1600	0,9	8,1	8,1	6,9	7,5	7,6	7,50	0,49
19	1600	1600	1,0	8,3	8,3	7,05	7	7	7,45	0,60
20	1800	1600	1,1	7,7	7,7	7,7	8,2	8,2	7,87	0,24
21	1000	1800	0,6	6,9	6,9	7,2	6	6	6,70	0,51
22	1200	1800	0,7	7,3	7,3	6,4	6,9	6,9	6,87	0,37
23	1400	1800	0,8	9,4	9,4	5,9	8,7	8,7	8,00	1,51
24	1600	1800	0,9	7,6	7,6	6	6,4	6,4	6,67	0,68
25	1800	1800	1,0	6,6	6,6	5,9	7	7	6,50	0,45

Figure 4.9: Heights of samples

Figure 4.9 presents height measurements at various positions of the sample, resembling thickness aspects. Extremely left, middle 1, middle 2 (central positions), middle 3, and finally extremely right. On the left side of the table, there are the average height and the standard deviation (SD) of height. Consequently, the laser power (P) is directly correlated with thickness as a result of more energy-promoting material being deposited per layer. However, increasing power does not always increase height, as material diffusion and melting behavior change at the power level. Finally, variations in height and thickness across measurements indicate the presence of thermal distortions or non-uniform material deposition under specific conditions [43].

ID	P [W]	v [mm/s]	LED (J/mm)	Length mm
1	1000	1000	1,0	51,1
2	1200	1000	1,2	51,3
3	1400	1000	1,4	51,3
4	1600	1000	1,6	51,2
5	1800	1000	1,8	51,4
6	1000	1200	0,8	51,2
7	1200	1200	1,0	50,8
8	1400	1200	1,2	51,5
9	1600	1200	1,3	51,1
10	1800	1200	1,5	51,3
11	1000	1400	0,7	46,1
12	1200	1400	0,9	50,9
13	1400	1400	1,0	51,0
14	1600	1400	1,1	51,1
15	1800	1400	1,3	51,2
16	1000	1600	0,6	40,8
17	1200	1600	0,8	50,7
18	1400	1600	0,9	51,4
19	1600	1600	1,0	50,8
20	1800	1600	1,1	51,1
21	1000	1800	0,6	50,9
22	1200	1800	0,7	50,8
23	1400	1800	0,8	50,9
24	1600	1800	0,9	51,1
25	1800	1800	1,0	51,3

Figure 4.10: Lengths of samples

Figure 4.10 presents the samples' lengths, most of them measurements around ~51 mm, and it indicates the dimensional stability. Two of the samples, which are marked in the color of dark orange, point out a short length respective to others. There was no significant relationship between laser power, scanning speed, and the final sample length, meaning their effects on longitudinal shrinkage or expansion were minimal.

Finally, variations in height and thickness across measurements indicate the presence of thermal distortions or non-uniform material deposition under specific conditions [43].

4.4 Sample Cutting Machine

In this context, during the characterization of the test, the initial step was the cutting machine, which can be seen in Figure 4.11 was used to cut the test sample from the build plates. The machine is a compact, wet abrasive precision cut-off machine. The cutting process was performed using a cermet blade with a continuous water supply to ensure cooling. The build plate, with the attached samples, was secured to the cutting bed via a clamp. The machine is equipped with a guiding laser that aligns the cutting blade with the intended cutting line. Then, both the feed rate of the cutting bed and the rotational speed of the blade are adjustable via the machine's control panel. These parameters must be configured so that the maximum current limit is not exceeded.

Figure 4.11: QATM Precision Cut-off machine (Model: Brilliant 220) [44]

Figure 4.12 depicts the cutting process that has been done in the DISAT laboratory. Following the completion of the cutting process, the cross-sectional specimens are placed inside the hot mounting machine.

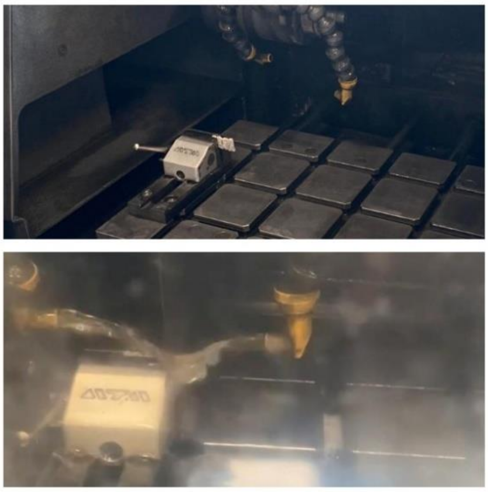

Figure 4.12: cutting process

4.5. Metallographic Hot Mounting Machine

In the mounting machine, the cross-section specimens are embedded in a resin. Figure 4.13 shows the hot mounting machine Remet IPA 30. The cut samples were held by means of metal clips (Figure 4.14), and then, a powdered resin was added to the chamber of the machine where the cut sample is placed (Figure 4.15). The chamber lid was closed, ensuring the whole chamber was heated up to its target temperature.

Figure 4.13: Remet Hot Mounting Machine [45]

Figure 4.14: Mounting clips and resin


Figure 4.15: cut-off sample in the chamber

Finally, the temperature of the chamber is allowed to decrease to room temperature, and then the chamber is depressurized. Therefore, the encapsulated sample is extracted from the machine. These samples are shown in Figure 4.16.

Figure 4.16: samples encapsulated in resin

4.6. Polishing Machine

The polishing machine, as shown in Figure 4.17, was used to remove scratches from the desired surface of the samples. After the mounting, the sample surfaces still contain scratches and deformation layers. Its main purpose is to ensure a smooth, scratch-free surface on the specimens [46]. In addition, mirror-like surfaces that are provided by a polishing machine assist in the next activity. Observing the microstructure when using an optical microscope at high resolution easily. Polishing machines generally function by means of a rotating disc, which is covered by cloths with abrasive suspensions such as silica solution [47]. Modern polishing machines include variable speed control and programmable sequences. We used to diverse grits of papers from lower to higher, respectively 400/800/1200/4000. The bed's rotational speed was kept at 100 rpm.

For instance, firstly, 400-grit paper was used to remove any burrs from the cutting process, and then polishing with this until all scratches disappear. Then, the platform was cleaned with water and continued with 800-grit paper with the orientation of the surface of the sample rotated by 90°. The same process was followed for the next polishing paper.

Figure 4.17: Presi automatic polishing machine [48]

4.7. Optical Microscope (OM)

An optical microscope (OM), which can be seen in Figure 4.18, operates using visible light and a system of optical lenses to magnify and resolve small features such as the specimen's surface, allowing observation of microstructural features such as grains or cracks of the polished samples, porosity, and phase distribution [49]. Moreover, the optical microscope is equipped with digital cameras and image analysis software to enable quantitative examinations. The OM networked to a computer and hence obtained images on its hard drive. The magnification ranges of the OM 5 up to 1000X, which is sufficient to study grain size, precipitates, and microstructural morphology. The example of the image is obtained from the OM (Figure 4.19)

Figure 4.18: Leica DMI Optical Microscope (Model: 5000M) [49]

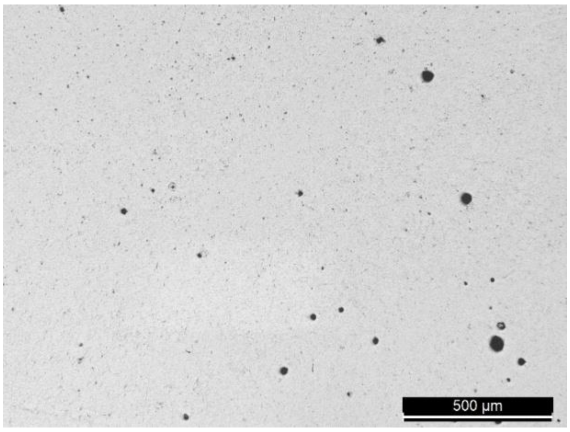

Figure 4.19: Image obtained from Optical Microscope

4.8. Image Analysis using ImageJ Software

In porosity analysis, Image J allows for quantification of the amount, size, shape, and distribution of pores in the imaged specimen. After obtaining the images by means of the optical microscope, we used this software to detect the porous area. The settings of this program as thresholding to clearly distinguish pores from the matrix of the image, and then calculating the porosity percentage. ImageJ gives area measurements in pixels; convert to physical units if calibration is available.

4.9. Scanning Electron Microscope (SEM)

A Scanning Electron Microscope (SEM), which is a specific of electron microscope to scans the surface and reveals the microstructure of a sample (Figure 4.20). It focuses a beam of electrons instead of a light beam to produce signals that give high-resolution image information. The machine operates in a vacuum and in a high depth of field, and thus, permits much more of the sample to be in focus. The working principle is different; firstly electron beam is generated by an electron gun, which functions as the cathode of the machine. In addition, it is accelerated by high voltage toward the sample, and the electron beam is emitted from a thermionic electron source. When the electron beam strikes the sample surface, various electrons and X-rays are emitted. For instance, for imaging purposes, back-scattered electrons (BSEs) and secondary electrons (SEs) are utilized. Furthermore, the thickness of the electron beam column can directly affect the resolution of the resulting image [50].

Figure 4.20: Scanning Electron Microscope (Phenom XL G2) [51]

5. Results and Discussion

5.1 Flowability

The flowability of the powder was measured using the Hall Flow method, as discussed in the context of the equipment used for characterising the powder. The test procedure was realized in Politecnico di Torino DISAT laboratory, and it was reported to be 13.0 ± 0.4 seconds/50 grams. Furthermore, with the procedure clarified in section 4, the bulk and tapped density values for the powder were calculated. ρ_{bulk} was calculated 4.6 ± 0.1 g/cm^3 and ρ_{tapped} was 6.3 ± 0.4 g/cm^3. The average values are within the threshold of excellent flow characteristics. Flowability ensures homogeneous powder distribution during layer deposition in additive manufacturing. This property is particularly critical for building thin-wall geometrical features, where insufficient powder flow could otherwise lead to defects, irregular wall thickness, or incomplete consolidation. Hence, the measured value confirms the suitability of the powder for producing complex geometries with high dimensional accuracy.

5.2 Microstructure of the Sample

5.2.1 Porosity Comparison of Samples

Initially, all samples' microstructures were observed by means of the optical microscope, in the following pages as demonstrated them.

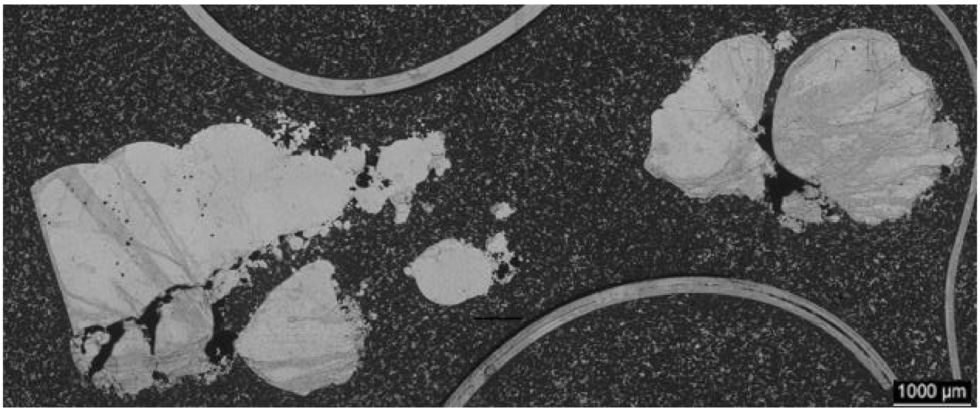

Figure 5.1: Sample 1

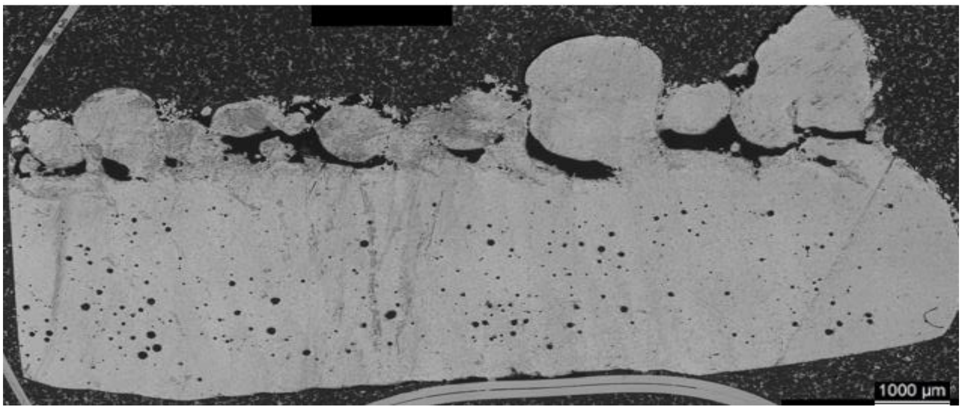

Figure 5.2: Sample 2

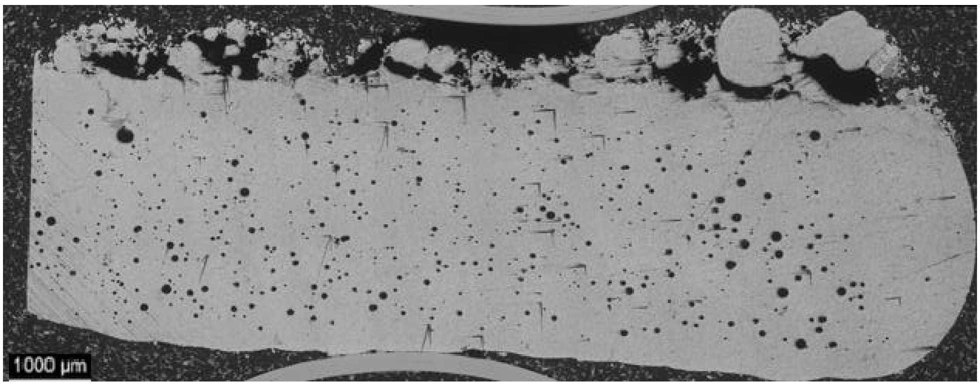

Figure 5.3: Sample 3

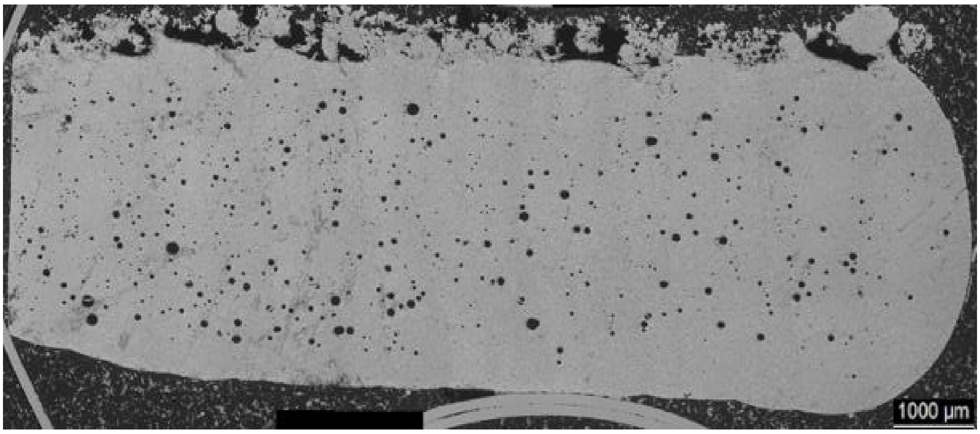

Figure 5.4: Sample 4

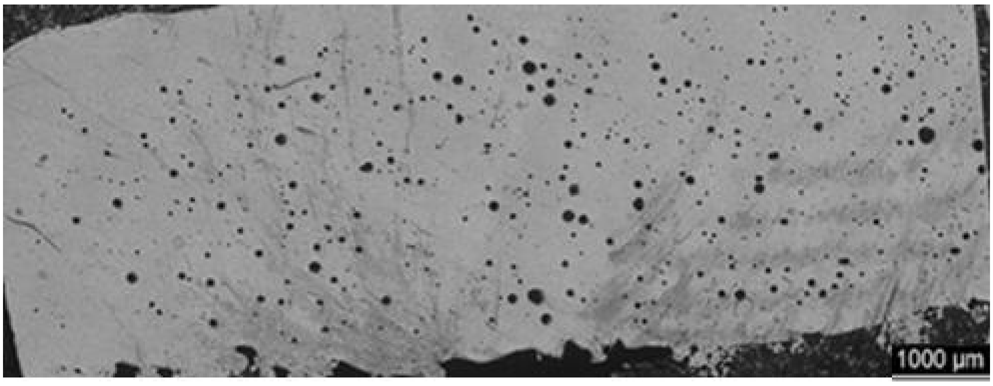

Figure 5.5: Sample 5

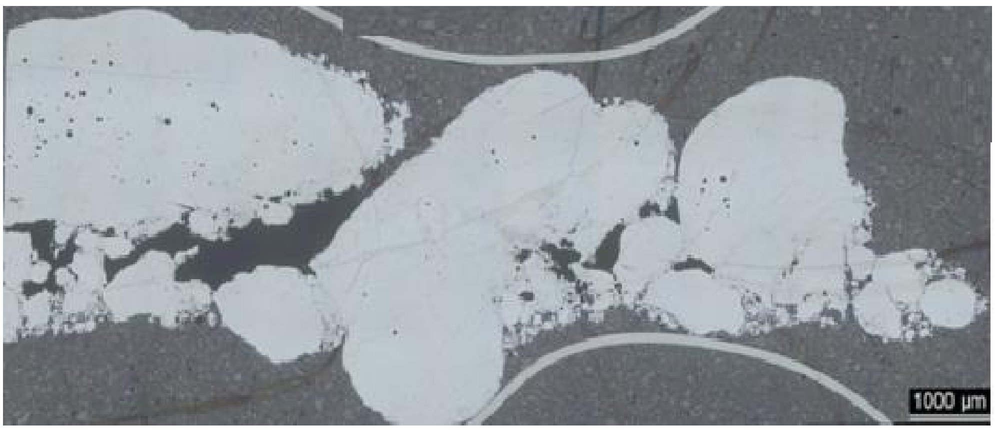

Figure 5.6: Sample 6

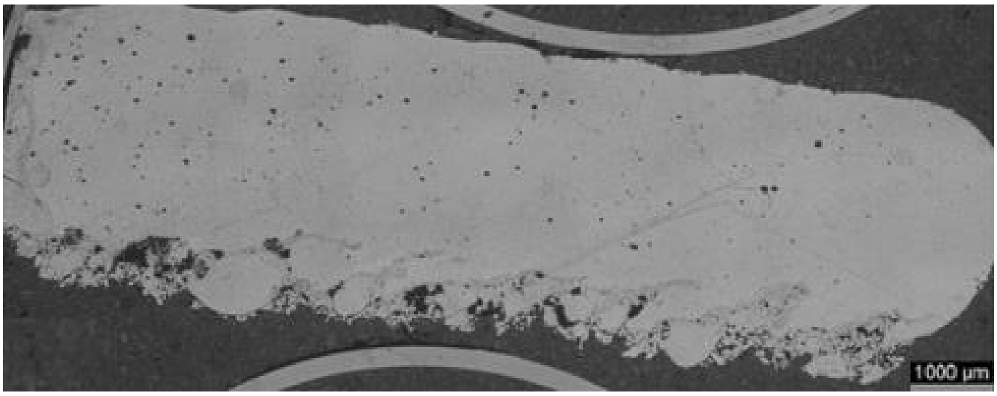

Figure 5.7: Sample 7

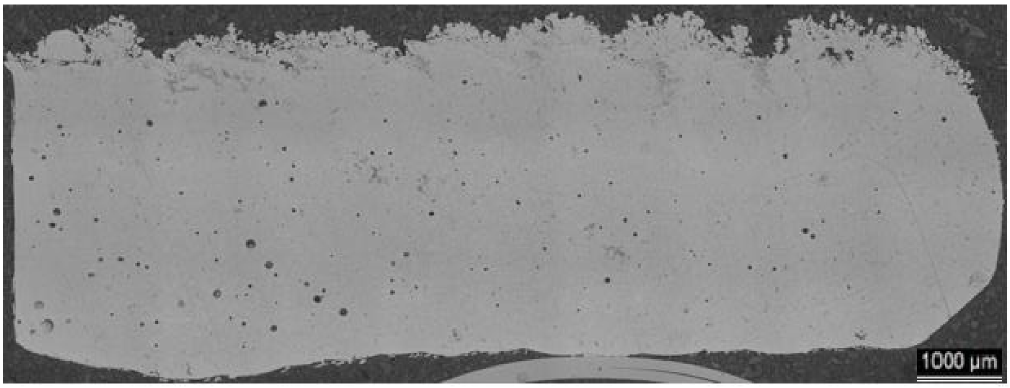

Figure 5.8: Sample 8

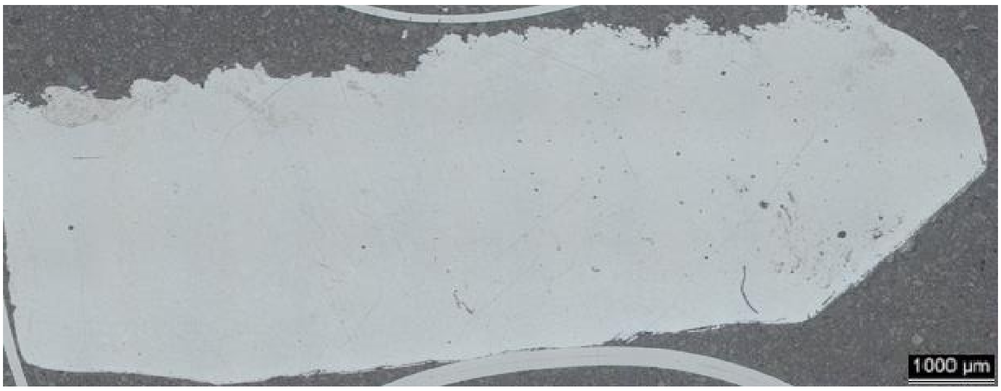

Figure 5.9: Sample 9

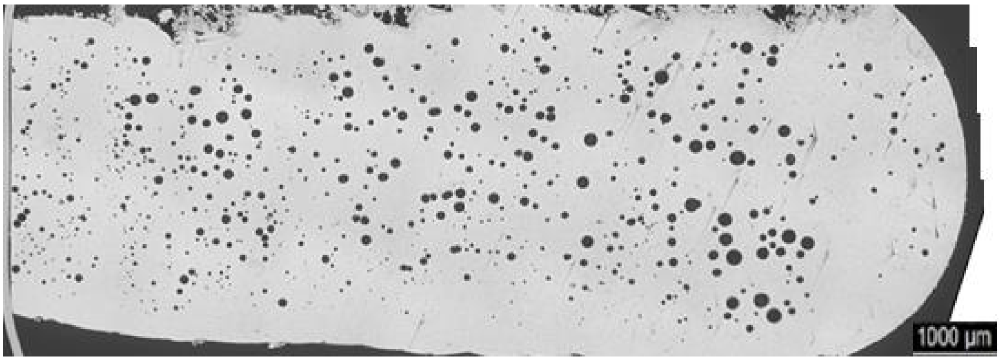

Figure 5.10: Sample 10

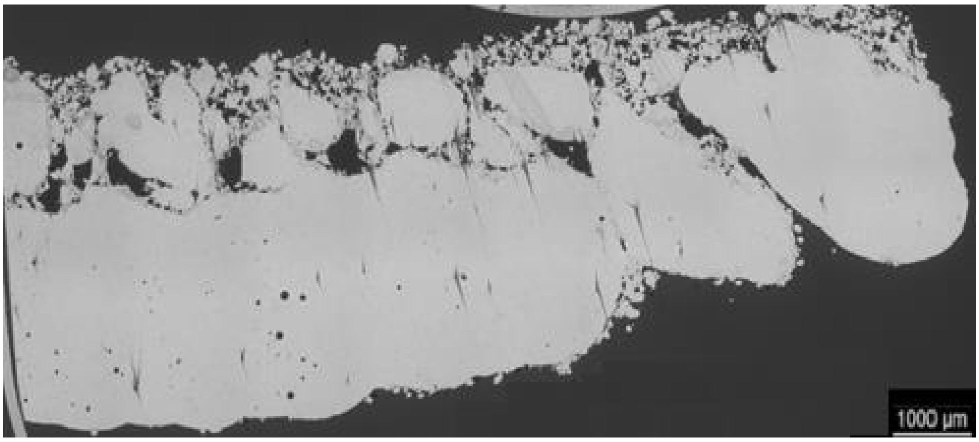

Figure 5.11: Sample 11

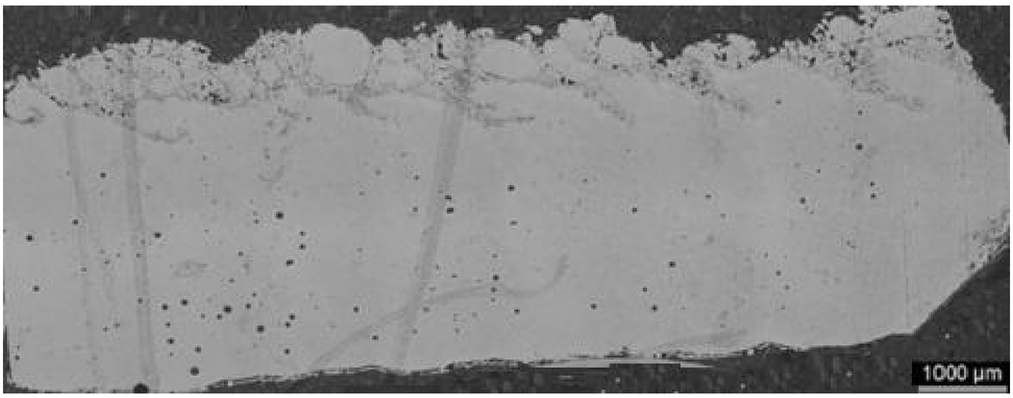

Figure 5.12: Sample 12

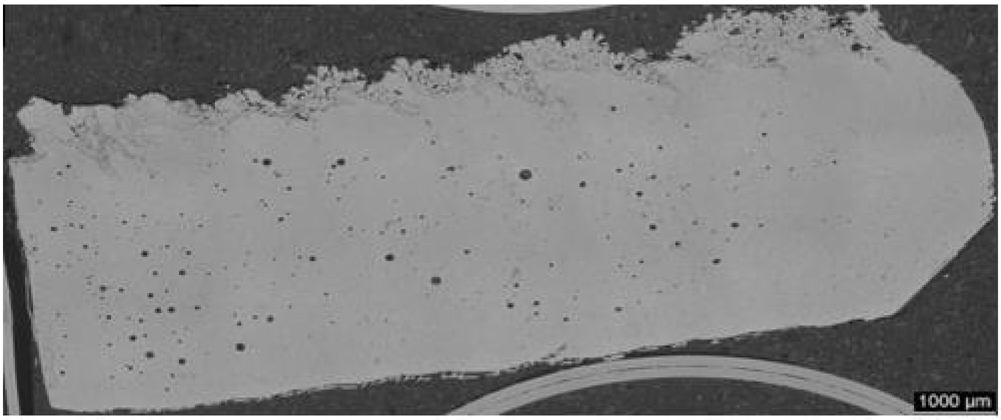

Figure 5.13: Sample 13

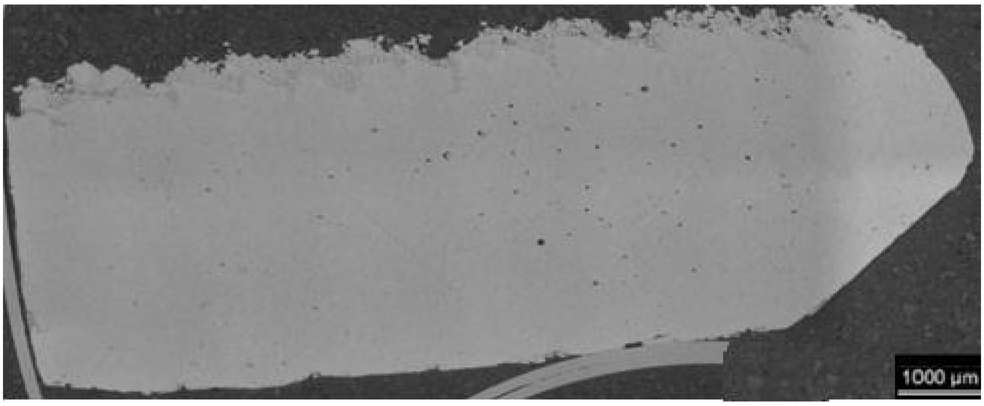

Figure 5.14: Sample 14

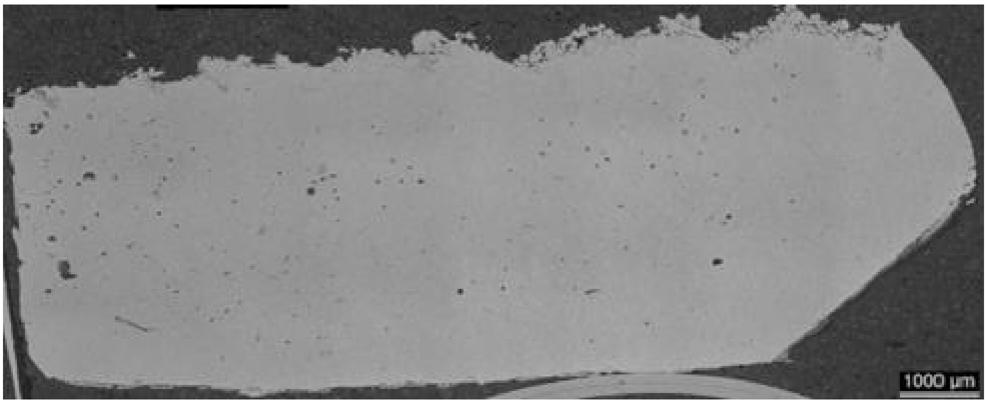

Figure 5.15: Sample 15

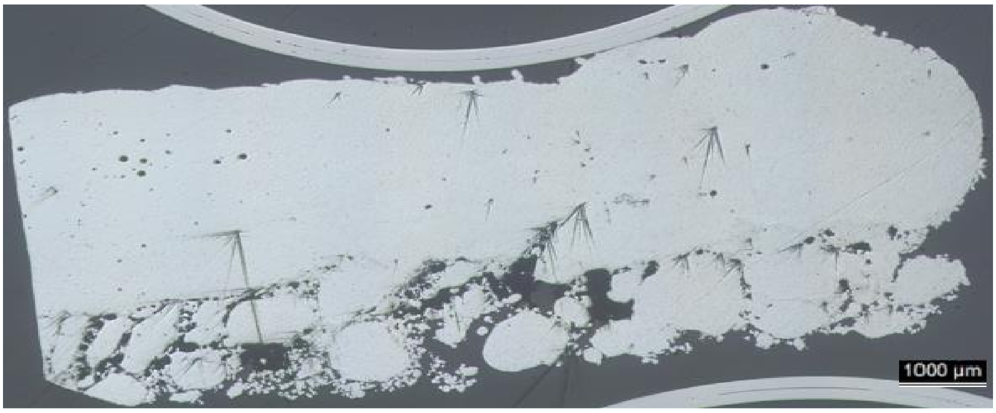

Figure 5.16: Sample 16

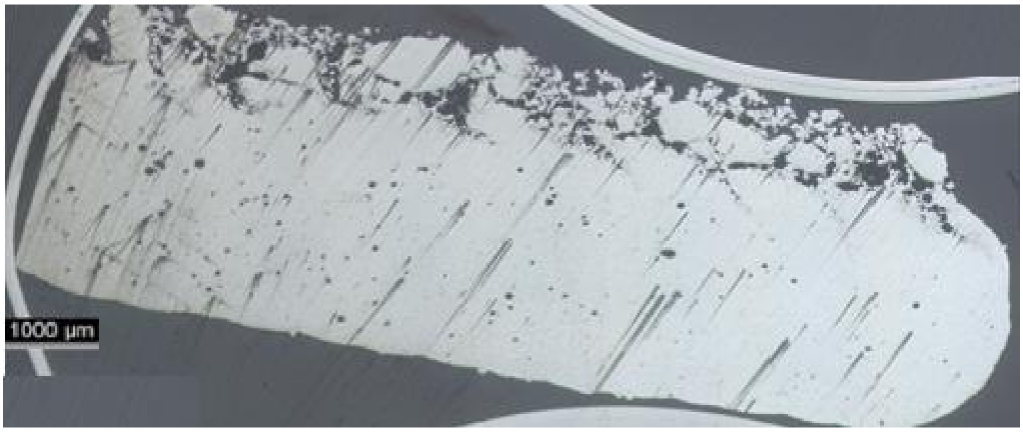

Figure 5.17: Sample 17

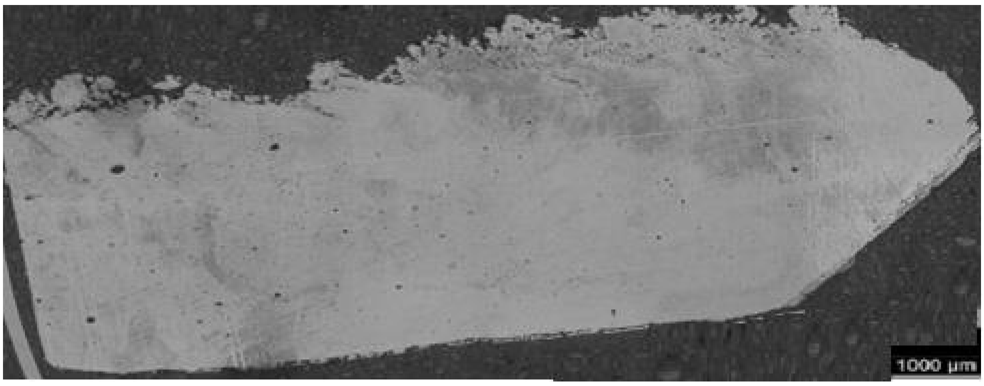

Figure 5.18: Sample 18

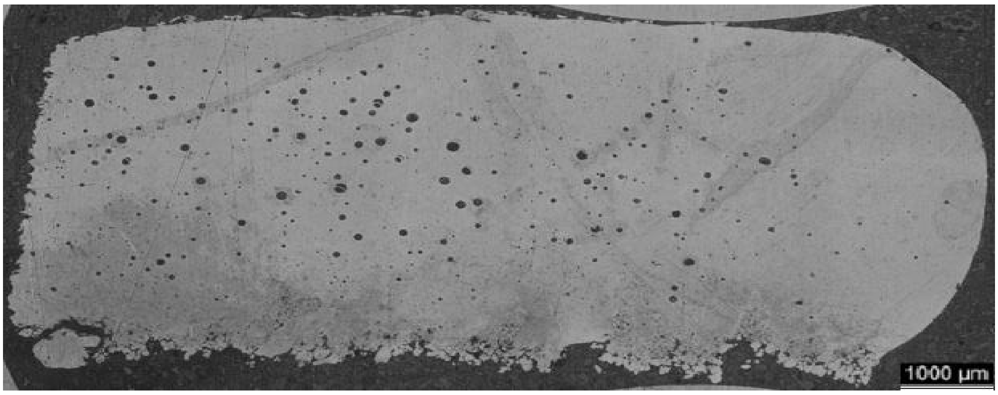

Figure 5.19: Sample 19

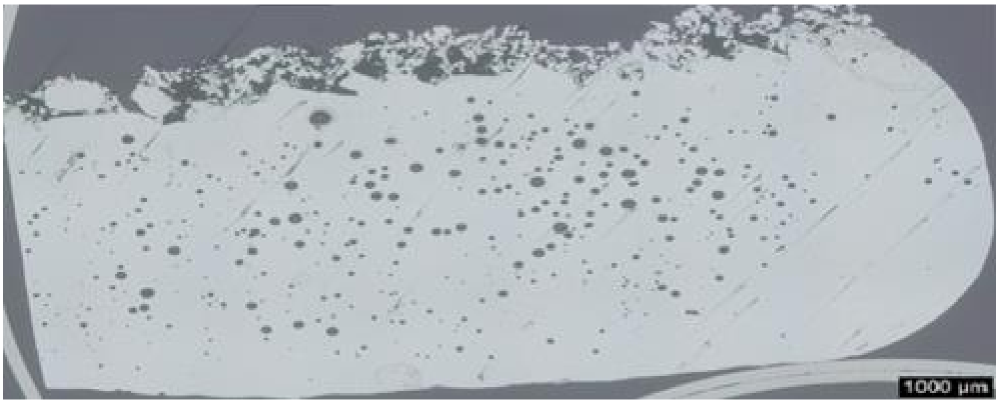

Figure 5.20: Sample 20

Figure 5.21: Sample 21

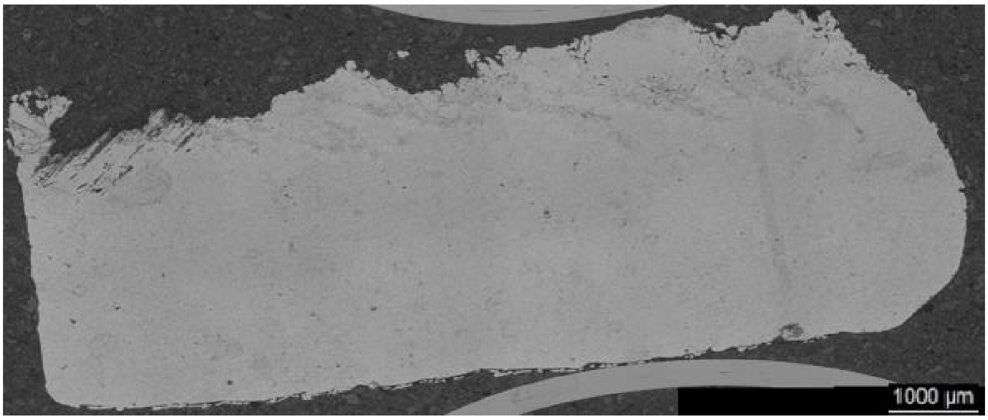

Figure 5.22: Sample 22

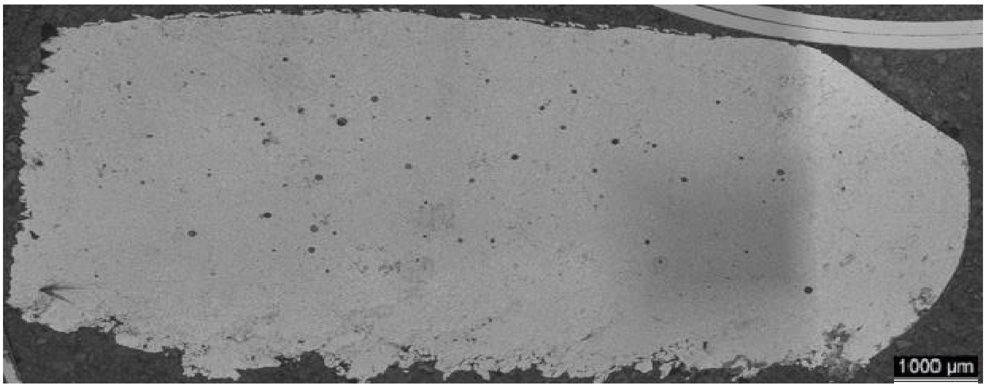

Figure 5.23: Sample 23

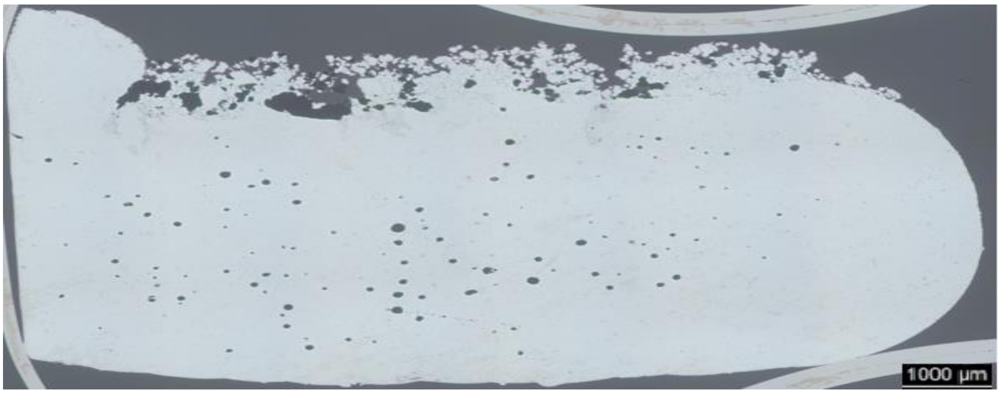

Figure 5.24: Sample 24

Figure 5.25: Sample 25

ID	P [W]	v [mm/s]	LED (J/mm)	Nr Pores	Total Area	Average Size	Area %	Mean	Circularity	Solidity
1	1000	1000	1	20637	0,34	1,65E-02	2,4	102.463	0,794	0,838
2	1200	1000	1,2	79842	1.945	2,44E-02	6,9	126.515	0,862	0,87
3	1400	1000	1,4	80027	2.264	2,83E-02	8,1	132.713	0,815	0,844
4	1600	1000	1,6	103022	2.455	2,38E-02	8,2	128.961	0,829	0,851
5	1800	1000	1,8	101619	3.611	3,55E-02	11,7	129.958	0,845	0,872
6	1000	1200	0,8	23836	0,849	3,56E-02	4,5	179.739	0,845	0,87
7	1200	1200	1	54034	0,717	1,33E-02	3,5	118.757	0,905	0,888
8	1400	1200	1,2	98876	1.094	1,11E-02	4,4	127.504	0,864	0,867
9	1600	1200	1,3	71046	1.062	1,50E-02	4,3	170.693	0,845	0,875
10	1800	1200	1,5	91285	2.844	3,12E-02	11,3	193.747	0,857	0,86
11	1000	1400	0,7	39644	0,868	2,19E-02	7,1	173.748	0,826	0,842
12	1200	1400	0,9	51089	0,967	1,89E-02	4,6	127.164	0,886	0,884
13	1400	1400	1	87315	1.085	1,24E-02	5,3	127.933	0,878	0,886
14	1600	1400	1,1	121329	0,954	7,86E-03	5	131.541	0,882	0,884
15	1800	1400	1,3	82898	0,683	8,25E-03	3,4	121.937	0,871	0,892
16	1000	1600	0,6	27605	0,915	3,32E-02	8,1	201.676	0,833	0,869
17	1200	1600	0,8	13941	0,786	5,64E-02	5,5	168.886	0,828	0,862
18	1400	1600	0,9	16925	0,237	1,40E-02	1,6	98.595	0,889	0,877
19	1600	1600	1	58441	1.272	2,18E-02	7,8	111.038	0,874	0,87
20	1800	1600	1,1	172374	3.606	2,09E-02	21,2	198.535	0,854	0,872
21	1000	1800	0,6	23359	0,529	2,27E-02	4,3	197.391	0,841	0,858
22	1200	1800	0,7	19076	0,138	7,24E-03	1,1	112.810	0,939	0,911
23	1400	1800	0,8	10438	0,152	1,45E-02	1,2	96.195	0,902	0,89
24	1600	1800	0,9	96021	1.331	1,39E-02	9,4	204.325	0,863	0,873
25	1800	1800	1	30283	0,829	2,74E-02	6	159.309	0,848	0,868

Figure 5.26: Result of ImageJ Analysis

The result of the ImageJ Software analysis, seen in figure 5.26, each column on the graph demonstrates that, respectively, laser power (P), scanning speed (v), and line energy deposition (LED), clarified in section 3.4 characteristic parameters of the DED. The number of pores is the total number of pores. Even if the pore count is high, each pore may be small, and in addition, a higher number highlights more porosity and potential weak points; in contrast, a lower number may depict better fusion and higher density.

Total area is the surface area of all detected pores, and this value represents the overall area occupied by pores within the sample. If the total area is high, the material density is reduced, and this affects mechanical properties. The average pore size, which means the size of the individual pores.

Large pores are more harmful than smaller pores due to occuring weak spots. The area percentage (%) represents the total porosity percentage, indicating that how much of the sample's cross-sectional area that consists of the pores. Porosity percentage is a crucial configuration in terms of the materials' mechanical properties. Moreover, the ideal porosity percentage is between 4-6 % which can be controlled; otherwise, the value is above 10% which can negatively affect the mechanical strength.

Furthermore, the area percentage and number of pores indicate that production parameters (P, v, and LED) affect the material integrity, while the measurement of the solidity and circularity provides insights into the information on the shape and structure of the pores. Hence, the ImageJ Analysis is considered to be an alternative method to estimate porosity by capturing the micro- and macro-pores in the given sample. Through the image analysis technique, porosity is estimated by executing image thresholding for the captured backscattered electron microscope images.

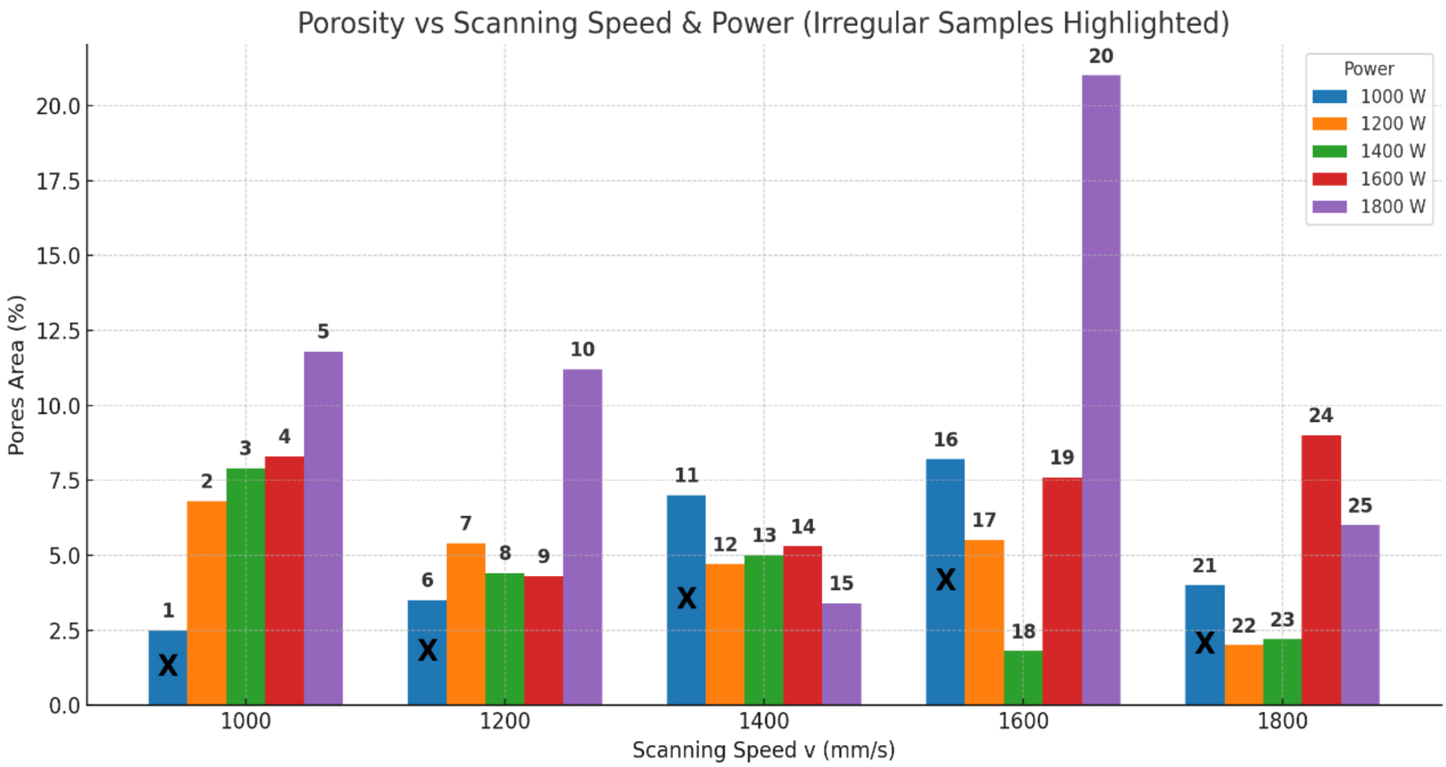

Figure 5.27: Pore Area % vs Scanning Speed & Power Graph

According to the ImageJ results, sample 20 has the highest pore area (21.2%), followed by ID 5, 10, and 24. Figure 5.27 illustrates the relationship between pores and process parameters, laser power (P) and scanning speed (v). Each scanning speed group (1000-1800 W) includes five individual samples, corresponding to different power levels (1000-1800 W). At low scanning speeds (1000 mm/s), especially combined with high power, pore percentage values exceed 10%. At intermediate scanning speeds (1400 mm/s), porosity appeared more stable across different power levels, with values mainly between 3% and 7%. At higher scanning speeds (1600-1800 mm/s), the porosity is less consistent. For instance, low porosity values (ID 18, 22, and 23), but sample 20, which reached over 21%. In addition, samples 1, 6, 11, 16, and 21, which exhibited non-continuous structures, are highlighted with marks (X) since evaluating process quality only based on porosity values may be misleading, and microstructural inspections must be considered in parallel.

The results demonstrate that the very high power or high scanning can destabilize the melt pool and increase gas entrapment, thus significantly raising the porosity.

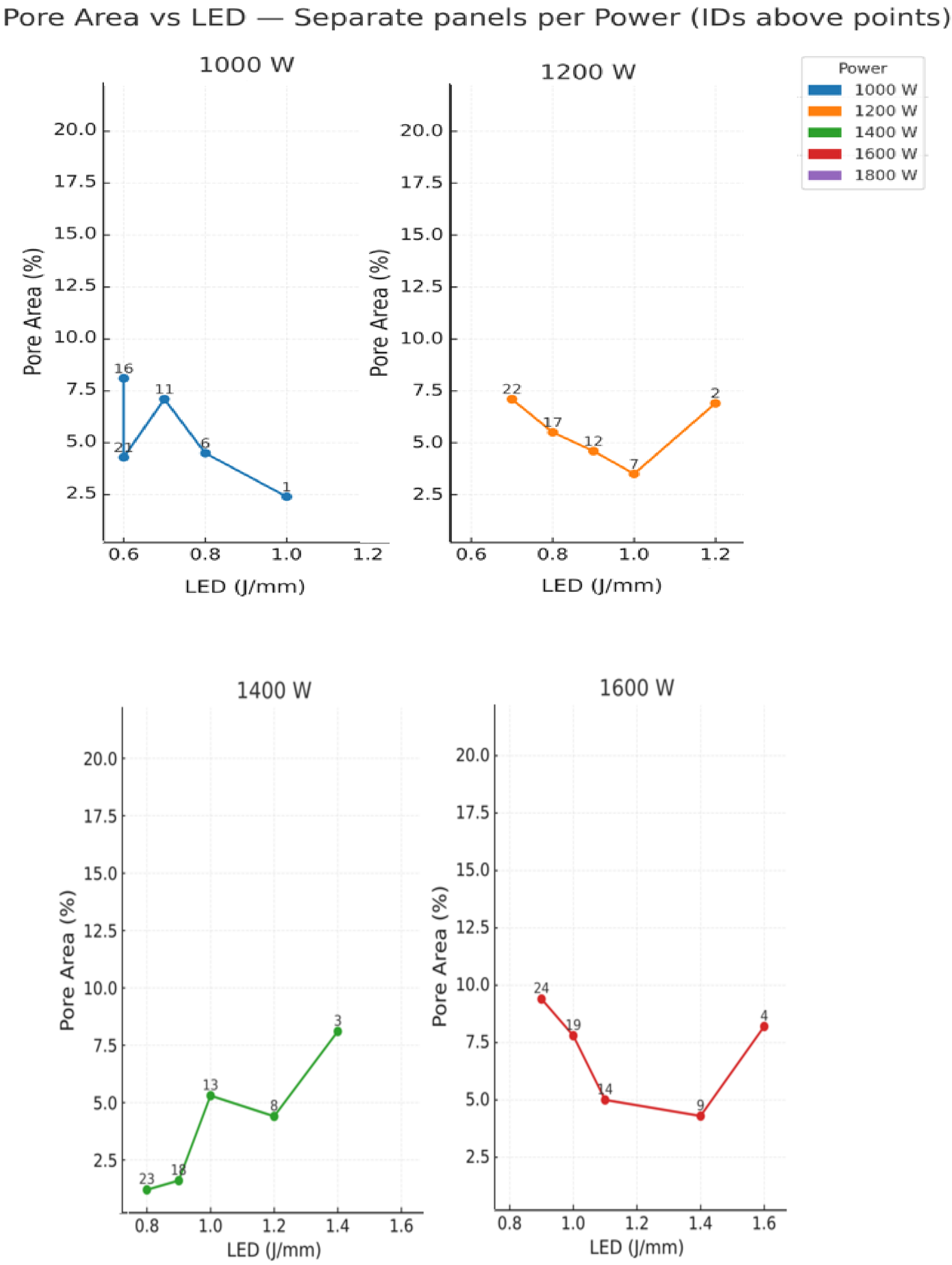

Figure 5.28: Pore Area vs LED & Power Graph-1-

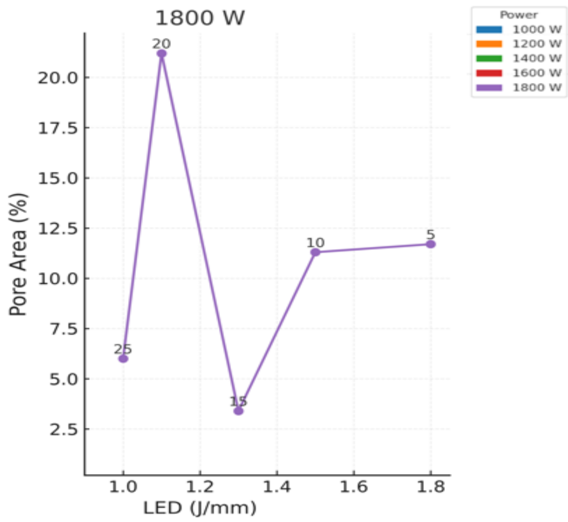

Figure 5.29: Pore Area vs LED & Power Graph-2-

In Figures 5.28 and 5.29, the separate graphs show that at low LED values, porosity levels remained relatively low for most samples; however, for higher powers, such as 1800 W, they resulted in increased pore area. At LED is 1.0 J/mm, porosity values were widely spread across the different powers, ranging from 3-8%. However, a remarkable peak was observed at the LED, which is 1.1 J/mm for the 1800 W, where porosity exceeded 20%. This sharp increase indicates that excessive energy input at this density induces keyhole porosity, highlighting the risks of operating at high power. Conversely, samples with power (1200-1400 W) at the same LED level demonstrated much lower porosity. Furthermore, as mentioned in the previous page, samples 1, 6, 11, 16, and 21 exhibited non-continuous structures are marked previous page. At higher LED values (>1.5 J/mm), porosity levels increased again, specifically under high power (1600-1800 W). Thus, this can cause overheating and excessive melt pool, which promotes pore entrapment. As a result, there is a non-linear correlation between porosity and LED; both insufficient and excessive energy densities led to pore formation, and therefore, optimization of LED and power is essential to reduce porosity.

As reported by ImageJ Analysis, pore density was calculated, and its relations with power, scanning speeds, and LED are shown below.

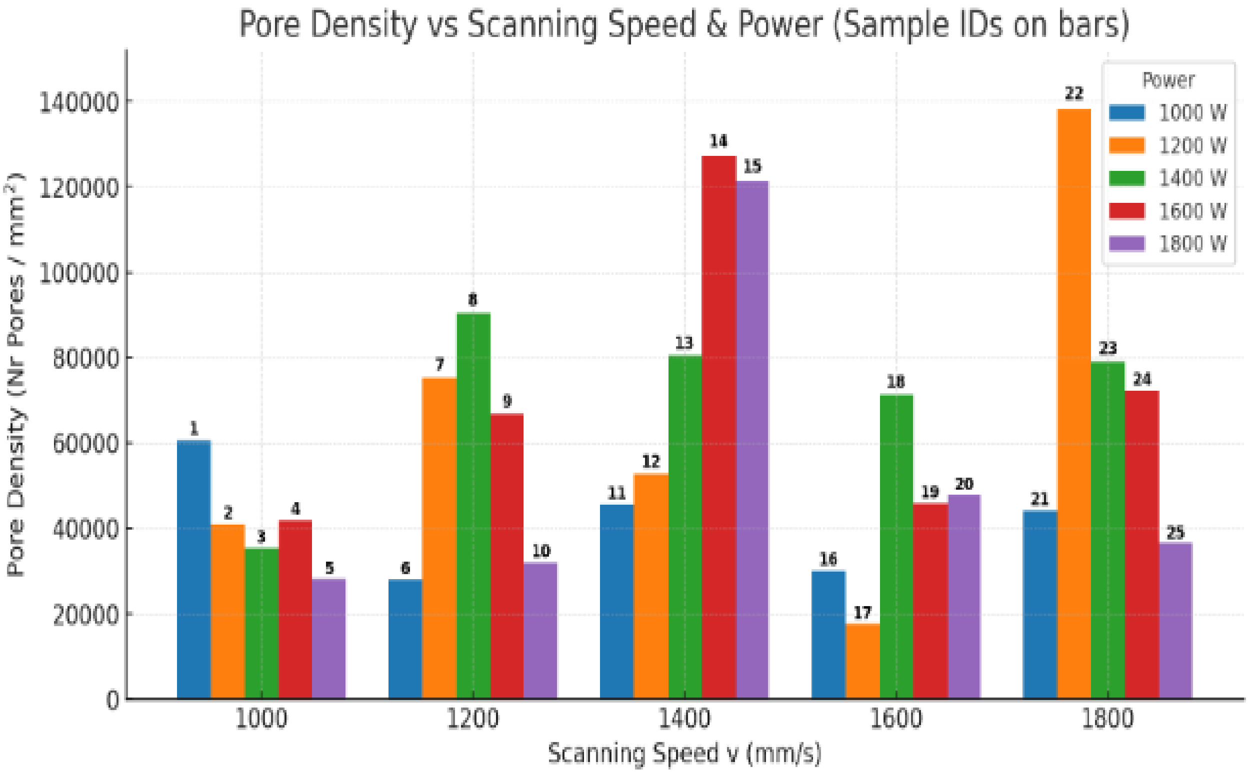

Figure 5.30: Pore Density vs Scanning Speed & Power Graph

The bar chart (Figure 5.30) shows that pore density varies non-linearly with scanning parameters. At low scanning speeds, pores are relatively fewer, but an irregular morphology is observed. At intermediate speeds, pore densities rise particularly in samples 14 and 15. At higher speeds, the overall trend is mixed. Samples 23 and 25 show only moderate pore densities. However, sample 22 is showing the highest pore density. Consequently, the combination of medium power with very high scanning speed creates pores, and cross-sectional images of samples (1-6-11-16-21) reveal irregularly shaped defects. Additionally, even if pore counts are not excessively high, defects may occur on the parts.

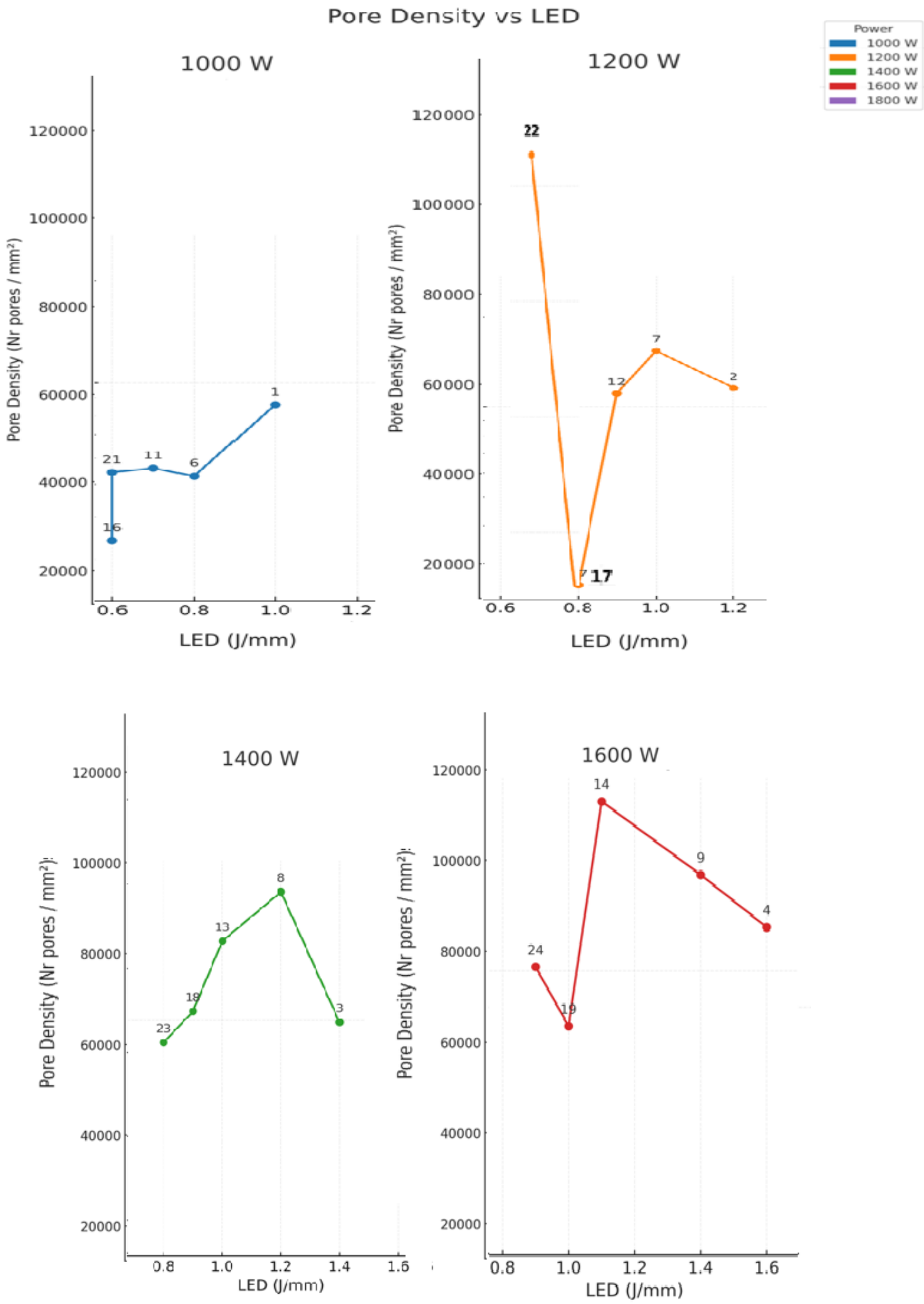

Figure 5.31: Pore Density vs LED & Power Graph-1-

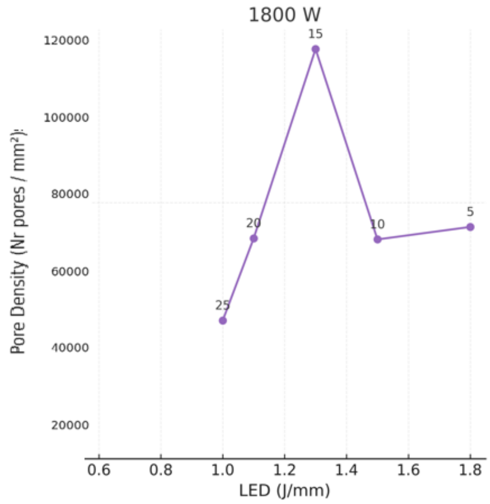

Figure 5.32: Pore Density vs LED & Power Graph-2-

Figures 5.31 and 5.32 demonstrate that, except for sample 22, the pore densities of all samples are generally low at low LED. Despite lower pore densities, samples (1-6-11-16-21) reveal irregularity. At moderate LED (0.9 – 1.2 J/mm), several critical points of instability are observed. For example, sample 14 reaches a relatively high density, depending on the applied laser power and line energy density (LED) parameters. At high LED, pore densities generally decrease, but irregular pore shapes can be visible. This indicates that too low LED levels cause a lack of fusion, while too high LED levels promote keyhole instability. The optimal range is between 0.9 and 1.0 J/mm, where pore densities can be minimized. Consequently, the results demonstrate that low pore area percentage does not necessarily correspond to low pore density. Instead, pore density highlights the prevalence of smaller pores that are not captured by area measurement. For example, sample 20 shows the highest pore area percentage (21.2%), but a comparatively lower pore density. The combined analysis of pore density provides a more comprehensive understanding of defect characteristics.

It depicts that both large volume pores and high-density small pores represent different but critical defects in terms of the mechanical performance of components. In addition, pore morphology is not only dependent on the energy density but also on the homogeneity of energy distribution within the melt pool. Under low power and low LED conditions, insufficient melting led to the formation of lack-of-fusion porosity, manifested by irregular pore shapes (notably in samples 1, 6, 11, 16, and 21)

5.2.2 Microstructural Characterization via SEM/EDS

Sample ID 18 was observed for microstructural details in terms of the material component by means of the SEM. A total of eight different regions of the same sample (ID 18) were observed. In Figure 5.31, one of the scans of sample 18, it can be seen that the microstructure reveals a dark-gray matrix containing bright-contrast elongated features, which are likely secondary phases or intermetallic compounds. The heterogeneous distribution and partial clustering of these features indicate microstructural non-uniformity. In addition, some dark round pores of varying sizes are visible, pointing to incomplete densification caused by insufficient melting, lack of fusion, or gas entrapment during the process.

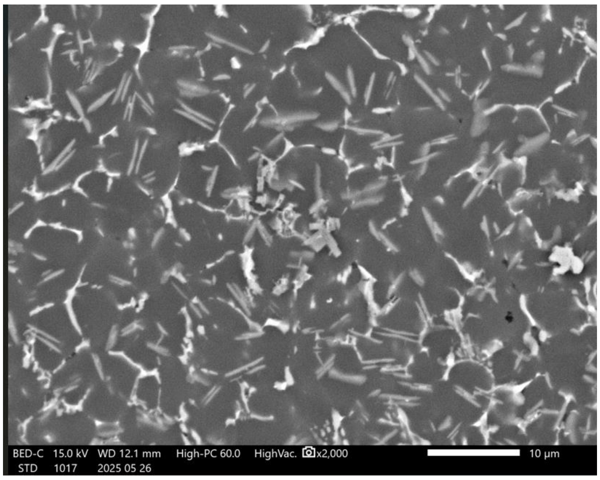

Figure 5.33: SEM/BED image of Sample ID 18

EDS point measurements were performed on the location of interest, and the results are shown in Figure 5.32 together with a morphological description and relative attributed phases. Elemental mapping detected that Al was uniformly distributed across the matrix, whereas Ti, B, Cu, and Ni were concentrated in localized regions.

Spectrum ID	Main Elements (WT %)	Secondary Elements (WT%)	Possible Phase	Morphology (SEM)
Spc_1	Al (58.3), Ti (25.9)	B (3.5), Mg (0.1), Cu (0.3)	**TiB_2 / Al-Ti-B**	Needle-like / clustered
Spc_2	Al (57.0), Ti (24.9)	B (3.6), Si (0.15), Cu (0.13)	**TiB_2 + Al matrix**	Elongated particles
Spc_3	Al (95.6)	Mg (0.9), Ti (0.34), Cu (1.5), Fe (0.4)	**Al-matrix + Al-Fe/Ti phases**	Matrix with fine containment
Spc_4	Al (96.5)	Mg (0.6), Si (0.04), Cu (1.0)	**Al-matrix + minor phases**	Mostly matrix, few precipitates
Spc_5	Al (96.4)	Mg (0.7), Ti (0.42), Cu (1.1)	**Al + Al-Ti/Cu phases**	Homogeneous with few containment
Spc_6	Al (68.5), Cu (15.5), Ni (6.8), Fe (5.6)	Mg (1.0), Si (0.9)	**Al-Cu-Ni-Fe intermetallics**	Irregular bright particles
Spc_7	Al (64.6), Cu (31.1)	Mg (1.2), Fe (1.5), Si (0.46)	**θ-Al_2Cu / Al-Cu intermetallics**	Large bright phases
Spc_8	Al (61.8), Cu (23.3), Ni (6.4), Fe (5.1)	Mg (1.2), Si (0.8)	**Al-Cu-Ni/Fe compounds**	Bright group particles

Figure 5.34: Result of SEM EDS analysis

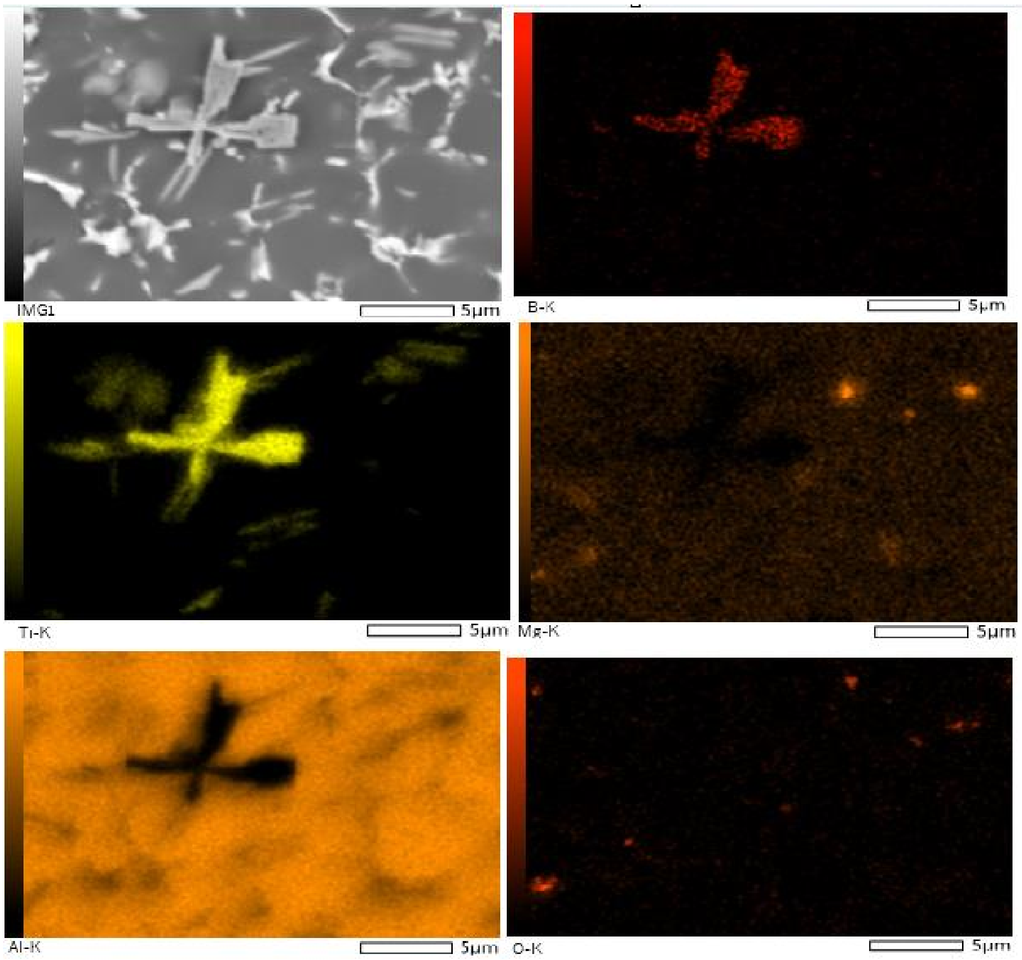

Figure 5.35: EDS elemental mapping of sample 18

In Figure 5.33, the presented EDS elemental maps provide insight into the chemical distribution of phases within the microstructure. B-K and Ti-K maps highlighted a strong enrichment of boron (B) and titanium (Ti) within the phase. Likely TiB_2 precipitates, which are commonly observed as needle- or cross-shaped morphologies in Al-based composites. The Al–K and Mg–K maps show a homogeneous background distribution, consistent with the Al–Mg matrix, where Al is the dominant element. The absence of significant enrichment of Mg within the irregular particle further supports that Mg remains primarily in solid solution or matrix phases rather than segregating into boride formations.

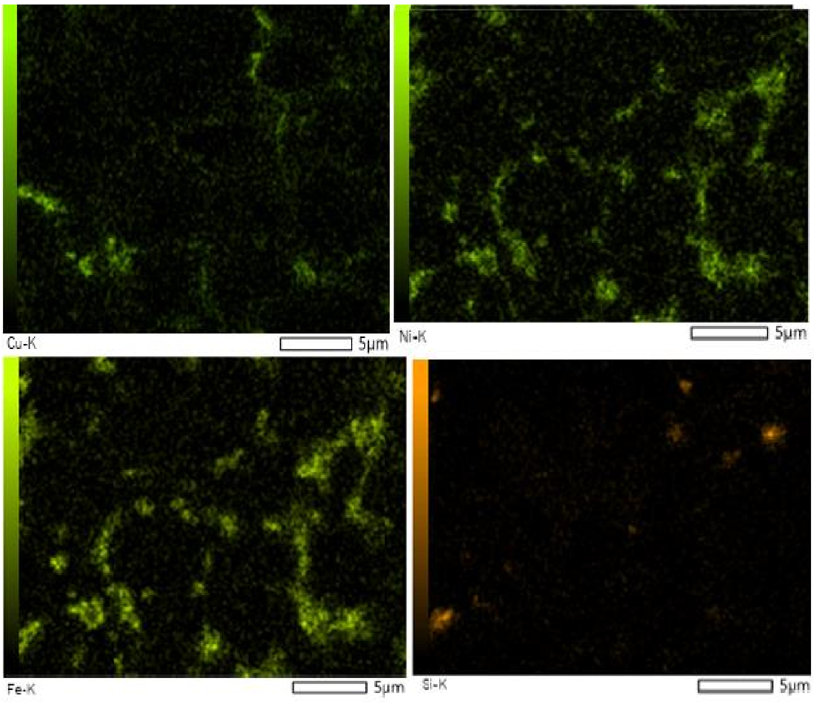

Figure 5.36: EDS elemental mapping of sample 18

Another Figure 5.34 illustrates that the Fe–K, Ni–K, and Cu–K maps reveal a dispersed distribution of these alloying elements, forming localized segregations at grain boundaries or interdendritic regions. These elements appear unrelated to the formation of the Ti–B-rich precipitate but may contribute to secondary strengthening phases in the microstructure. The Si–K signal is weak, showing only minor localized segregation, consistent with residual trace phases. Overall, the maps confirm that the irregular cross-shaped particle is a Ti–B-rich phase, specifically a TiB_2 precipitate, embedded within the Al–Mg matrix. Its sharp and well-defined morphology is consistent with the rapid solidification conditions during processing. The uniform Al background and dispersed Fe, Ni, and Cu signals highlight the complex multi-elemental environment of the alloy, but the dominant strengthening contribution is attributed to the TiB_2 precipitate.

6. CONCLUSIONS

To sum up, in a total of twenty-five Al-based (A2618+Ti+B) samples, the effect of processing parameters such as laser power, scanning speed, and linear energy density (LED) on porosity characteristics and microstructural features of the samples was investigated. The results from the pore area and pore density analyses demonstrated that power, scanning speed, and line energy density (LED) have a significant role in defect formation. While higher power levels generally increased the total pore area, the density did not always follow a similar tendency, indicating that a smaller number of larger pores can dominate porosity percentage, whereas numerous smaller pores can lead to high pore density despite a low pore area percentage. The highlights the importance of evaluating pore area and pore density to fully understand defect behavior. Moreover, insufficient energy input promotes incomplete melting and unstable melt pool dynamics, leading to the formation of irregularly shaped voids. The SEM and EDS analyses showed that the aluminum matrix remained the base element (65-97 wt%), while secondary phases such as Ti and B-rich precipitates (TiB_2), as well as Al_2Cu, Al–Cu–Ni, and Al–Fe intermetallic compounds. Moreover, TiB_2 precipitates may enhance hardness and wear resistance. The clustured intermetallics, particularly those enriched in Cu, Fe, and Ni, act as stress concentrators and are likely to correlate with the higher porosity.

Briefly, optimization of power and scanning speed is critical to balance between sufficient energy input for complete melting and the avoidance of excessive keyholing that increases pore size and density. Pore evolution in this system is governed by a combination of process dynamics (power–speed interaction controlling LED and melt pool stability) and elemental segregation (B- and Ti-rich phases stabilizing irregular pores). To minimize porosity and suppress irregular morphologies, an optimal processing window should avoid both extremely low LED (which leads to incomplete fusion) and excessively high scanning speeds (which destabilize melt pool flow). Furthermore, the role of reinforcing and intermetallic phases, such as TiB_2 and Al-(Fe, Ni, Cu), should be carefully considered since they directly influence microstructural stability and defect behavior.

References

[1] Charles Hull SLA invention', https://www.historyofinformation.com/detail.php?id=3864.

[2] Gibson, I., Rosen, D., & Stucker, B. (2021). *Additive Manufacturing Technologies: 3D Printing, Rapid Prototyping, and Direct Digital Manufacturing*. Springer.

[3] A. Gebhardt and J.-S. Hoetter, 'Rapid Tooling', in CIRP Encyclopedia of Production Engineering, L. Laperrière and G. Reinhart, Eds. Berlin, Heidelberg: Springer Berlin Heidelberg, 2014, pp. 1025–1035. doi: 10.1007/978-3-642-20617-7_16751.

[4] 'AM market size predictions 2030', https://www.grandviewresearch.com/industryanalysis/ additive-manufacturing-market.

[5]https://www.researchgate.net/figure/Typical-additive-manufacturing-processing-steps

[6] W. Tao and M. Leu, *Design of lattice structure for additive manufacturing*. 2016. doi: 10.1109/ISFA.2016.7790182

[7] M. Attaran, 'The rise of 3-D printing: The advantages of additive manufacturing over traditional manufacturing', Bus Horiz, vol. 60, no. 5, pp. 677–688, 2017, doi: https://doi.org/10.1016/j.bushor.2017.05.011

[8] A. Salmi, P. Minetola, and A. Saboori, "Additive Manufacturing Systems and Materials," Course Slides- Politecnico di Torino, 2019.

[9] Wakjira, Y., Akessa, A., & Lemu, H. (2021). Overview study on challenges of additive manufacturing for healthcare applications. *IOP Conference Series: Materials Science and Engineering, 1201*, 012041. https://doi.org/10.1088/1757-899X/1201/1/012041

[10]*The Seven Categories of Additive Manufacturing Technologies*.(2023, April 7). Default.https://altair.com/blog/articles/the-seven-categories-of-additive-manufacturing-technologies

[11] www.custompartnet.com/wu/3d-printing.

[12] Gibson, I., Rosen, D. and Stucker, B., 2014, Additive manufacturing technologies: 3D printing, rapid prototyping, and direct digital manufacturing, Chap. 5, Springr, New York, pp. 107-146.

[13] https://www.empa.ch/web/coating-competence-center/selective-laser-melting.

[14] https://www.lboro.ac.uk/research/amrg/about/the7categoriesofadditivemanufacturing/materialextrusion/

[15] Gibson, I., Rosen, D. and Stucker, B., 2014, Additive manufacturing technologies: 3D printing, rapid prototyping, and direct digital manufacturing, Chap. 7, Springer, New York,pp 175-204.

[16] DebRoy, T., et al. (2018). "Additive Manufacturing of Metallic Components – Process, Structure and Properties." *Progress in Materials Science*, 92, 112–224

[17] Hatch, J.E., *Aluminum: Properties and Physical Metallurgy*, ASM International, 1984

[18] Mondolfo, L.F. (1976). *Aluminum Alloys: Structure and Properties*. Butterworths.

[19] Totten, G.E., & Mackenzie, D.S. (2003). *Handbook of Aluminum: Vol. 1 Physical Metallurgy and Processes*. CRC Press.

[20] Prasad, N.E., & Wanhill, R.J.H. (2014). *Aerospace Materials and Material Technologies*. Springer.

[21] Polmear, I.J. (2006). Light Alloys: From Traditional Alloys to Nanocrystals. Butterworth-Heinemann.

[22] DebRoy, T., et al. (2018). "Additive Manufacturing of Metallic Components – Process, Structure and Properties." *Progress in Materials Science*, 92, 145–224.

[23] Kumar, S., et al., "Grain refinement of aluminum alloys by TiB_2 particles," *Materials Science and Engineering A*, 528 (2011): 5516–5522.

[24] Zhao Shouxin, Yangxun Ou, Hongying Li (2016) Synthesis, microstructure, and mechanical properties of in situ TiB2/Al-4.5Cu composites

[25]https://www.makeitfrom.com/material-properties/2618A-2618A T851AlCu2Mg1.5Ni

[26] G.Lupi, L.Mariotti, A.Mistrini, J.Larsson, L.Patriarca, R.Casati, (2025) Microstructure and tensile properties of TIB2-reinforced Al-2618 thin walls produced by laser powder bed fusion

[27] Dávila, J., Neto, P., Noritomi, P., Coelho, R., & Silva, J. (2020). Hybrid manufacturing: A review of the synergy between directed energy deposition and subtractive processes. *International Journal of Advanced Manufacturing Technology, 110.*

[28] S. L. Sing, C. F. Tey, J. H. K. Tan, S. Huang, and W. Y. Yeong, " - 3D printing of metals in rapid prototyping of biomaterials: Techniques in additive manufacturing," in *Rapid Prototyping of Biomaterials (Second Edition)*, Second Edition., R. Narayan, Ed. Woodhead Publishing, 2020, pp. 17–40

[29] Gibson, I., Rosen, D. and Stucker, B., 2014, Additive manufacturing technologies: 3D printing, rapid prototyping, and direct digital manufacturing, Chap. 10, Springer, New York, pp. 245-268

[30] F. Wirth, S. Arpagaus, and K. Wegener, "Analysis of melt pool dynamics in laser cladding and direct metal deposition by automated high-speed camera image evaluation," Additive Manufacturing, vol.21, pp. 369–382, May 2018, doi: 10.1016/j.addma.2018.03.025.

[31] https://www.spilasers.com/application-additive-manufacturing/what-is-laser-metal-deposition

[32] Frazier, W. E. (2014). Metal additive manufacturing: a review. *Journal of Materials Engineering and Performance*, 23(6), 1917–1928. https://doi.org/10.1007/s11665-014-0958-z

[33] Herzog, D., Seyda, V., Wycisk, E., & Emmelmann, C. (2016). Additive manufacturing of metals. *Acta Materialia*, 117, 371-392. https://doi.org/10.1016/j.actamat.2016.07.019

[34] Pinkerton, A.J. (2015). *Int. J. Machine Tools & Manufacture*, 78, 1–12.

[35] King, W.E. et al. (2015). *Laser powder bed fusion additive manufacturing: physics of complex melt flow and instability*. Applied Physics Reviews, 2(4), 041304.

[36]Slanalytical.com/materials-matter/advanced-powder-flowability-testing--additive-manufacturing.

[37]http://www.labulk.com/astmb212-free-flowing-metal-powdersapparent-density-hall-flowmeter-funnel/.

[38] Standard Test Methods for Flow Rate of Metal Powders Using the Hall Flowmeter Funnel 1 2. Referenced Documents 2.1 ASTM Standards: 2 B215 Practices for Sampling Metal Powders B243 Terminology of Powder Metallurgy B855 Test Method for Volumetric Flow Rate of Metal Powders Using the Arnold Meter and Hall Flowmeter Funnel B964 Test Methods for Flow Rate of Metal Powders Using the Carney Funnel, doi: 10.1520/B0213-13.

[39] ASTM Standards B215 Practices for Sampling Metal Powders B243 Terminology of Powder Metallurgy B873 Test Method for Measuring Volume of Apparent Density Cup Used in Test Methods B212, B329, and B417 E456 Terminology Relating to Quality and Statistics.

[40]Standard Test Method for Tap Density of Metal Powders and Compounds B215 Practices for Sampling Metal Powders B243 Terminology of Powder Metallurgy E177 Practice for Use of the Terms Precision and Bias in ASTM Test Methods E691 Practice for Conducting an Interlaboratory Study to Determine the Precision of a Test Method

[41] ASTM Standards B215 Practices for Sampling Metal Powders B243 Terminology of Powder Metallurgy E177 Practice for Use of the Terms Precision and Bias in ASTM Test Methods E691 Practice for Conducting an Interlaboratory Study to Determine the Precision of a Test Method

[42] Anton Paar Pycnometer (Model: Ultrapyc 5000)', *https://www.anton-paar.com/usen/products/details/ultrapyc/*

[43]Zhang, Y., Liou, F. W., & Seufzer, W. J. (2017). *Laser additive manufacturing of metallic components: materials, processes and mechanisms*. International Journal of Advanced Manufacturing Technology, 91(1-4), 1–14.

[44]PRECISION CUT-OFF MACHINE BRILLANT 220'. Accessed: Sep. 09, 2022. [Online]. Available:https://www.qatm.com/dltmp/www/c62ebbb2-c432-4d23-9f80-52a16fc491c6-65685c7174be/brochure_cutting_brillant220_en.pdf

[45] Remet compression mounting press IPA 30', https://www.bqc.be/en/metallography/hotmounting/mounting-presses/hot-mounting-press-ipa-30-mm/a-5849-20000432

[46] Vander Voort, G. F., *Metallography: Principles and Practice*, ASM International, 2007

[47] Buehler, *Metallographic Sample Preparation Guide*, 2020.

[48] Lapping and Polishing Machine'. Accessed: Sep. 09, 2022. [Online]. Available: https://www.mcscorpusa.com/wp-content/uploads/2019/02/Poloshing-Machines-MECATECH-234-264-mcscorpusa-English.pdf

[49] 'Leica DMI 5000M', https://www.leica-microsystems.com/products/light-microscopes/p/leicadmi5000-m/gallery/.

[50] Thermo Fisher Scientific. (n.d.). *Phenom XL G2 Desktop SEM*. Retrieved from

[51] Alfatest Phenom XL G2 Scanning Electron Microscope', *https://www.alfatest.it/prodotti/phenom-xl-sem-da-banco*